Universidade de Campinas
Instituto de Computação

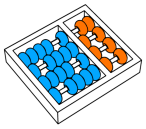

Raoni Florentino da Silva Teixeira

A new framework for quality assessment of high-resolution fingerprint images

Um novo arcabouço para análise de qualidade de imagens de impressões digitais de alta resolução

CAMPINAS
2015

Universidade de Campinas
Instituto de Computação

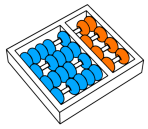

Raoni Florentino da Silva Teixeira

A new framework for quality assessment of high-resolution fingerprint images

Um novo arcabouço para análise de qualidade de imagens de impressões digitais de alta resolução

Thesis presented to the Institute of Computing of the University of Campinas in partial fulfillment of the requerements for the degree of Doctor in Computer Science.

Tese apresentada ao Instituto de Computação da Universidade Estadual de Campinas como parte dos requisitos para a obtenção do título de Doutor em Ciência da Computação.

Supervisor/Orientador: Prof. Dr. Neucimar Jerônimo Leite

Este exemplar corresponde à versão final da Tese defendida por Raoni Florentino da Silva Teixeira e orientada pelo Prof. Dr. Neucimar Jerônimo Leite.

CAMPINAS
2015

Agência(s) de fomento e nº(s) de processo(s): CAPES, 01-P-3951/2011; CNPq, 147050/2012-0

Ficha catalográfica
Universidade Estadual de Campinas
Biblioteca do Instituto de Matemática, Estatística e Computação Científica
Maria Fabiana Bezerra Muller - CRB 8/6162

T235n

Teixeira, Raoni Florentino da Silva, 1987-
A new framework for quality assessment of high-resolution fingerprint images / Raoni Florentino da Silva Teixeira. – Campinas, SP : [s.n.], 2016.

Orientador: Neucimar Jerônimo Leite.
Tese (doutorado) – Universidade Estadual de Campinas, Instituto de Computação.

1. Biometria. 2. Processamento de imagens. 3. Sistemas de imagem - Qualidade de imagem. I. Leite, Neucimar Jerônimo,1961-. II. Universidade Estadual de Campinas. Instituto de Computação. III. Título.

Informações para Biblioteca Digital

Título em outro idioma: Um novo arcabouço para análise de qualidade de imagens de impressões digitais de alta resolução
Palavras-chave em inglês:
Biometrics
Image processing
Imaging systems - Image quality
Área de concentração: Ciência da Computação
Titulação: Doutor em Ciência da Computação
Banca examinadora:
Neucimar Jerônimo Leite [Orientador]
Leyza Elmeri Baldo Dorini
Aparecido Nilceu Marana
Ricardo da Silva Torres
André Santachè
Data de defesa: 29-01-2016
Programa de Pós-Graduação: Ciência da Computação

Universidade de Campinas
Instituto de Computação

Raoni Florentino da Silva Teixeira

A new framework for quality assessment of high-resolution fingerprint images

Um novo arcabouço para análise de qualidade de imagens de impressões digitais de alta resolução

Examining Committee:

- Prof. Dr. Neucimar Jerônimo Leite
  IC/Unicamp
- Profa. Dra. Leyza Elmeri Baldo Dorini
  DAINF/UTFPR
- Prof. Dr. Aparecido Nilceu Marana
  FC/Unesp
- Prof. Dr. Ricardo da Silva Torres
  IC/Unicamp
- Prof. Dr. André Santanchè
  IC/Unicamp

A ata da defesa, onde constam as assinaturas dos membros da banca, está arquivada pela Universidade Estadual de Campinas.

Dedication

I would like to dedicate this work to my beloved wife, Ana. Definitively, I would not have done this work without her.

“Eu queria fazer parte das árvores como os pássaros. Eu queria fazer parte do orvalho como as pedras. Eu só não queria significar. Porque significar limita a imaginação. E com pouca imaginação eu não poderia fazer parte de uma árvore. Como os pássaros fazem. Então a razão me falou: o homem não pode fazer parte do orvalho como as pedras fazem. Porque o homem não se transfigura senão pelas palavras. E isso era mesmo..." (Manuel de Barros)

Acknowledgements

This work is part of a long process of maturation. My family, my advisor (who was a model for me during these graduate school days), my friends, and colleagues (some people I had the pleasure of meeting at UEMS, Unicamp, UFMT, and so on) were essential in this process.

I am grateful to all of these people, as well as to all the institutions and companies that provided funding for this research, namely Unicamp, UFMT, CAPES, CNPq, and FAPESP. In special, I also need to thank everyone in Brazil who indirectly helped me with financial support. Thank you.

Resumo

A falta de robustez referente à degradação de qualidade de conjuntos de características extraídas de padrões de cristas-e-vales, contidos na epiderme dos dedos humanos, é uma das questões em aberto na análise de imagens de impressões digitais, com implicações importantes em problemas de segurança, privacidade e fraude de identificação. Neste trabalho, introduzimos uma nova metodologia para analisar a qualidade de conjuntos de características de terceiro nível em imagens de impressões digitais representados, aqui, por poros de transpiração. A abordagem sugerida leva em conta a interdependência espacial entre as características consideradas e algumas transformações básicas envolvendo a manipulação de processos pontuais e sua análise a partir de ferramentas anisotrópicas. Foram propostos dois novos algoritmos para o cálculo de índices de qualidade que se mostraram eficazes na previsão da qualidade da correspondência entre as impressões e na definição de pesos de filtragem de características de baixa qualidade a ser empregado num processo de identificação. Para avaliar experimentalmente o desempenho destes algoritmos e suprir a ausência de uma base de dados com níveis de qualidade controlados, criamos uma base de dados com diferentes recursos de configuração e níveis de qualidade. Neste trabalho, propusemos ainda um método para reconstruir imagens de fase da impressão digital a partir de um dado conjunto de coordenadas de poros. Para validar esta idéia sob uma perspectiva de identificação, consideramos conjuntos de minúcias presentes nas imagens reconstruídas, inferidas a partir das configurações de poros, e associamos este resultado ao problema típico de casamento de impressões digitais.

Abstract

The lack of robustness against the quality degradation affecting sets of features extracted from patterns of epidermal ridges on our fingers is one of the open issues in fingerprint image analysis, with implications for security, privacy, and identity fraud. In this doctorate work we introduce a new methodology to analyze the quality of sets of level-3 fingerprint features represented by pores. Our approach takes into account the spatial interrelationship between the considered features and some basic transformations involving point process and anisotropic analysis. We propose two new quality index algorithms, which have proved to be effective as a matcher predictor and in the definition of weights filtering out low-quality features from an identification process. To experimentally assess the performance of these algorithms and supply the absence of a feature-based controlled quality database in the biometric community, we created a dataset with features configurations containing different levels of quality. In this work, we also proposed a method for reconstructing phase images from a given set of pores coordinates. To validate this idea from an identification perspective, we considered the set of minutia present in the reconstructed images and inferred from the pores configurations and used this result in fingerprint matchings.

List of Figures

List of Tables

Contents

Chapter 1

Introduction

Security, privacy, and identity fraud are some of today's most widely discussed and controversial issues. In terms of modern economy and technology, the debate about these questions revolves mainly around a mechanism for human identification in an automatic and unique manner. A concrete example in this sense is given by the great number of applications requiring users to be securely authenticated (e.g., e-commerce, e-trading, homeland security, personal data protection). This concern has naturally revived the interest in biometric techniques and, in particular, in fingerprint recognition, mainly due to the interesting properties commonly attributed to fingerprints, namely, *universality*, *permanence*, *collectability*, and *distinctiveness* [33].

In order to satisfy these requirements, Automated Fingerprint Identification Systems (AFIS's) were created and became very popular. The automatic recognition performed by an AFIS relies on an accurate extraction of some features derived from fingerprint patterns. Unlike traditional image processing approach, the term feature here is related to specific details of the fingerprint pattern (e.g., minutiae, pores). In many practical applications, these features can be also combined with other representation schemes including, among others, images of gray-scale values [3], phase [54] and skeletons [16, 19].

Usually, an AFIS works under different non-controlled conditions due to the potential number of users and the inappropriate handling of the attached sensor. As a consequence, several degradation factors can affect the quality of all aforementioned representation schemes. That is the case of degradations caused by physical skin injuries, inconsistent contact and unwanted residues on the sensor surface which result in a loss of quality of the original information. Further, we can add errors concerned with parameters estimation during the steps of image preprocessing, segmentation, and feature extraction and/or other modules concerned with the identification system. All these factors are closely related to the final set of obtained fingerprint features [1, 30, 32].

Since some of these operations cannot be controlled or avoided, the issues of quality assessment of both captured image and extracted features became progressively more important in the last few years. Although great progress has been made in the last few decades (see Chapter 2, for a brief review), prior works are generally limited in the sense that they are based mainly on the iconic representation and conditions of the input images [1, 5, 9, 22, 26, 30, 32, 41, 45, 49, 59].

In general, the concepts behind the image-based quality indexes currently available

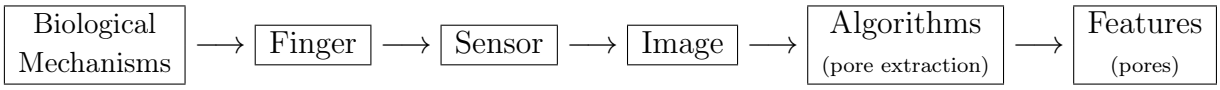

Figure 1.1: Hypothesis of our framework. We assume that feature distribution on high-quality samples are imposed by some biological mechanisms acting on the fingerprint formation.

in literature (see Chapter 2, for a review) have a straight visual correspondence with the clearness of the ridges. Nevertheless, they are not well adapted to cope with problems related, for example, with the inaccurate estimation of the parameters by feature extraction algorithms (e.g. ridge direction [30]). Indeed, one of the most important problems with this type of index concerns the lack of robustness against the quality degradation affecting directly the set of related features. Further, since different photometric properties are closely dependent on the image acquisition, any image-based quality measure may work differently, according to the used capture sensor [1].

This doctorate work focuses on a new type of quality assessment which considers not only the gray-scale image information but also the set of extracted features represented by the pores present in high-quality fingerprint images. Such an objective quality index can improve the overall system efficiency in two ways. First, it can be used to assist on the feature extraction or provide a quality feedback about the image acquisition process. Second, this quality information can assign confidence levels to the extracted features during a matching phase or be used in conjunction with other biometric features. As it will be illustrated in the experiments (Chapter 6), a fingerprint matching algorithm can take advantage of this information by defining weights such that low-quality features are partly considered in the identification process.

Our research hypothesis is that

quality approaches can take advantage of feature distribution due to biological mechanisms (see Figure 1.1) to improve the identification performance.

More specifically, we explore in this work the fact that competitive interactions among the pores coordinates can be used to analyze the quality of set of pores and improve the identification.

1.1 Main contributions

In this thesis we present a new methodology to analyze the quality of sets of fingerprint features. Our approach is based on the interrelationship between features locations, their manipulation via spatial transformations, and some tools for anisotropic analysis. These main contributions can be grouped into the following three classes:

- *Modeling*: The contribution in this category relies on models taking into account the way sweat pores arise on fingertips. We design a model for the mechanism regarding

the spatial interaction of the fingerprint sweat pores from an energy-optimization standpoint. We also propose an approach for reconstructing the phase image from a given set of pores coordinates. The assumption in this case is that fingerprint ridges do arise along a minimum-energy path linking distinct pores. These contributions were tested for a consistent set of real fingerprint images and the results obtained from experiments corroborate the efficacy of the models.

- *Algorithmics*: In this aspect we illustrated how well-known techniques from different areas of literature (e.g., meshing, numerical optimization, statistics, probability theory) can be integrated to approach the problem of fingerprint quality assessment. In particular, we introduced a framework yielding the design of two new feature-based quality algorithms dealing with spatial and structural properties of the fingerprint features distribution. Two main questions guided this study: (i) are the locations of the extracted features plausible? and (ii) is the set of extracted features coherent with other available information drawn from the captured image? The proposed quality index algorithms based on these questions have proved to be effective in the definition of fingerprint image quality indexes, in the sense that they can be used as a predictor in a typical matching procedure.

- *Experimental*: The main contributions here comprises methodological way to assess feature-based quality indexes and improve the performance of pore-based matching. In this sense, we designed a new feature-based quality dataset with features configuration containing different levels of quality. This dataset supplies the absence of a feature-based controlled quality database in the biometric community. Furthermore, from an identification point of view, we proposed two new approaches relying on the idea of features carrying complementary information (e.g., minutiae) to the one supplied by pores, and use such a combination in matching algorithms. Namely, we show that minutia can be inferred from the reconstructed phase images encompassed by our proposed structural algorithm and used to improve pore-based identification. We also define an adaptive strategy to combine matching scores obtained from sets of pores and corresponding inferred minutia, based on the quality of a given features configuration.

1.2 Thesis Organization

We organized the remainder of this thesis in six chapters. Chapter 2 examines the literature for related work. Chapter 3 gives a brief overview of previous theoretical thinking necessary for the understanding of this thesis. Chapter 4 describes the steps of our basic framework, and Chapter 5 contains the main contributions related to the original algorithms for feature-based quality assessment. Chapter 6 shows the experimental protocol used to validate our work and corresponding results. Finally, Chapter 7 draws conclusions about our techniques, describes strengths and shortcomings, and gives perspectives of future and on going research.

Chapter 2

Related Work

This chapter examines the literature for related work. We look at connections of our work with modern fingerprint techniques and discuss some of the major approaches available for fingerprint quality.

2.1 Literature Review

Fingerprints are orientated texture patterns created by interleaved ridge and valley information present on fingertip surfaces. Modern literature about these patterns dates back to the late sixteen century with the work by N. Grew [18], which is believed to be the first one in this area to introduce a systematic analysis about ridges, furrows, and pores structures. Since then, a certain number of researchers have invested significant efforts in studying this subject [10, 17, 20, 21, 24, 33, 37–39, 43, 46, 52, 53, 58, 60] and, in the early twentieth century, fingerprints were formally accepted as valid mechanisms for human identification by law-enforcement agencies around the world [33]. Nowadays, Automatic Fingerprint Identification Systems (AFIS) are one of the most widely used technology for personal recognition, mainly due to the following attributes [33]:

- *Universality*: everyone has it.
- *Permanence*: remains invariant over lifetime.
- *Collectability*: easy to be collected.
- *Uniqueness*: it is sufficiently different from one person to another, even in cases of identical twins [25].

The purported uniqueness of fingertip patterns is characterized by three levels of features [8, 38]. Naturally, a finer analysis taking into account more distinguishable subsets of features might yield a more reliable identification. Level-1 features refer to singular points, such as cores and deltas illustrated in Fig. 2.1, around which the ridge orientation is discontinue or changes abruptly [24, 42]. Level-2 features is commonly related to local ridge discontinuities named minutia [22, 40, 47, 57]. Fig. 2.2 shows an example of two of the most prominent types of minutia, namely ridge ending (Fig. 2.2a) and bifurcation (Fig. 2.2b). The last and most distinguishable level is represented by fine intra-ridge

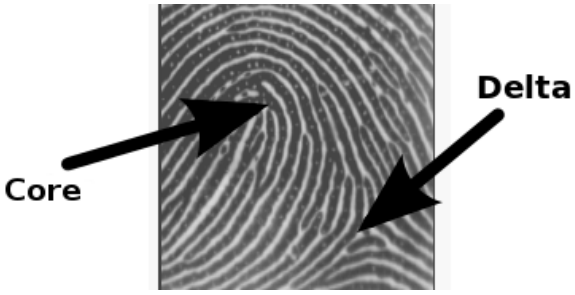

Figure 2.1: Core and delta in a fingerprint fragment.

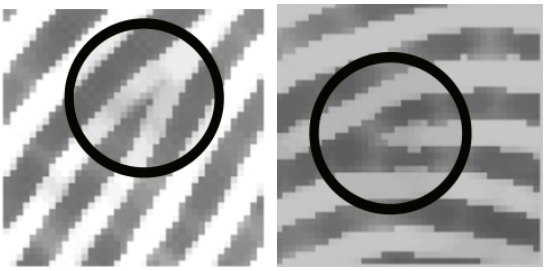

(a) (b)

Figure 2.2: Examples of minutiae: (a) ridge ending; (b) ridge bifurcation.

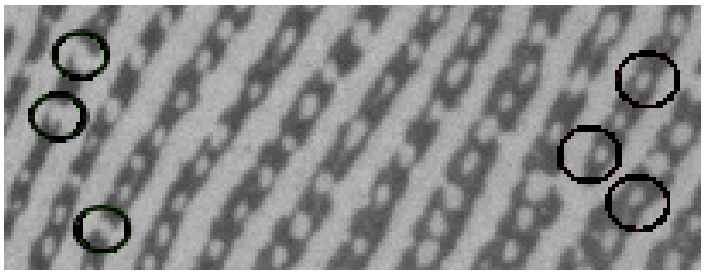

Figure 2.3: Example of fingerprint pores. Open and closed pores are marked, respectively, on the left and right side of the image.

details such as the fingertip sweat pores [23, 52, 53, 60]. Fig. 2.3 depicts some open and closed pores in a fingerprint fragment. As illustrated in this figure, the so-called closed pores are entirely enclosed by a ridge, while open ones intersect with a valley.

The main topic of this work concerns feature-based quality assessment system. Broadly, for the identification, an AFIS extracts sets of features and produces a real value indicating the similarity score between two fingerprints. Since an AFIS works under non-controlled conditions, the issues of quality assessment of both captured image and extracted features became progressively important in the last few years. Although great progress has been achieved, prior works are generally limited in the sense that they are based mainly on the iconic representation (gray-scale values) and conditions of the input images [1, 5, 9, 22, 26, 30, 32, 41, 45, 49, 59].

According to the quality assessment level, these approaches can be roughly classified into *local* or *global*. The former class, constituting the majority of the existing algorithms, takes a gray-scale fingerprint image and defines a quality map for blocks (or individual pixels) of the input image, at a given position. In general, the quality measure defined

here considers some fingerprint photometric information about the clarity of the ridges and valleys and the corresponding extractability of the considered features.

Lee *et al.* [30], for example, proposed a block-wise algorithm based on the shapes of probability density functions of 2D gradients. These functions are computed on two distinct subsets of image pixels: one parallel and the other perpendicular to the flow orientation of the ridges. The model in [30], soon followed by other works [1], explores the statistical relationship between the gray levels along the directional orientation of the ridges and the pixels in a perpendicular direction.

Hong *et al.* [22] modeled the ridges and valleys representation as a sinusoidal-shaped wave adjusted along the direction perpendicular to the corresponding flow orientation. The amplitude, frequency and variance of this wave are used to compute the quality of each image block.

More recently, Sutthiwichaiporn and Areekul [49] introduced a frequency-domain algorithm, which computes the fingerprint quality by considering the distinctiveness between ridges and noise signals. This approach takes into account the FFT applied to small image blocks and can be summarized into two steps. First, the noise and ridge signals are estimated and the region quality is computed as the ratio between the spectral values characterizing these signals. Locally, the ridge signal is related to the highest peak in the spectrum, while regions with spectral information below to this peak are related to noise.

Approaches based on learning of dictionaries have also been discussed in literature. In particular, Cao *et al.* [5] introduced a multi-scale approach to estimate the local quality of a gray-scale fingerprint image. This work is based on a dictionary of expected fingerprint patches representing distinct image regions. The patches are generated by a supervised learning taking into account image blocks with different directions and frequencies. The multi-scale estimation, in this case, is obtained by considering image blocks of different sizes. For the 500 dpi image resolution in [5], coarse and fine level qualities are defined from image blocks of size 64×64 and 32×32, respectively. At each scale, the quality is estimated through the structural similarity [56] between the expected patches and the image blocks extracted from the input image. The final quality is obtained by combining coarse and fine estimates into a single image.

The *global* methods characterizing the second type of image-based quality assessment yield a scalar value corresponding to the estimated quality of the whole input image. These approaches take advantage of some structural properties of the overall fingerprint patterns, as it is the case of the work by Chen *et al.* [9], which introduced a frequency-domain algorithm based on the concentration of energy in a ring-shaped region of the spectrum. The authors explore the fact that the frequency values of the ridges in a fingerprint image lie within a certain range. It is also expected that low-quality images have a diffuse distribution of energy while high-quality ones exhibit a concentration of energy in a few bands only. A set of bandpass filters computes the energy at each frequency and the entropy is used to evaluate the energy concentration.

Lim *et al.* [32] proposed two global indicators taking into account the continuity of the directional and frequency fields. The first indicator measures the abrupt changes occurring along the adjacent blocks of the directional field and is based on the observation that the ridge direction changes smoothly in high-quality images. The second one measures the

standard deviation of the ridge and valley trickiness ratio. The assumption here is that large deviations across the whole image can be associated with low-quality fingerprints while small deviations represent high-quality ones.

The widely-considered work by Tabassi and Wilson [50] introduces a global algorithm based on the degree of separation between match and non-match distributions of a given fingerprint. The rationale behind this approach is that low-quality samples are generally associated with scenarios where either there are few features or the features locations rely on image regions where the ridges are not distinguishable. The quality of a given input image is defined as a predictor of separation between match and non-match distributions. This prediction is accomplished by using a neural network by considering the distinctness of ridges, the amount of minutia and a minutiae quality-value (i.e., ridge distinctness at each minutiae position). The output of this network is a number that classifies the quality of the fingerprint into five values: 1 (excellent), 2 (very good), 3 (good), 4 (fair), and 5 (bad).

To sum up, the concepts behind the aforementioned image-based quality indexes are simple to understand and have a straight visual correspondence with the clearness of the ridges. Nevertheless, they are not well adapted to cope with problems related, for example, with the inaccurate estimation of the parameters. Indeed, one of the most important problems with this type of index concerns the lack of robustness against the quality degradation directly affecting the set of related features. Furthermore, since different photometric properties are closely dependent to the image acquisition, any image-based quality measure may work differently, according to the capture sensor [1]. To deal with these limitations, we will introduce a new type of quality assessment in the succeeding chapters.

Since this work relies on the spatial interrelationship between level-three features represented by pores, we briefly review two main results in literature about pore spatial distribution. Before proceeding, we should remember that the spatial distribution of these features depends on the initial biological environment from which the fingerprints have been developed [21, 27, 28, 39]. It is worth noting that the biological mechanisms involved in this process are still not completely elucidated and there is no consensus on how the arrangements of features arise [27, 28].

The first important result about pore spatial distribution is by Sir F. Galton's remark [17, chap. 4] asserting that usually the distance between successive pores on a ridge is directly proportional to their width. [1] The other important property concerns the well-known *regularity* of fingerprint pores. According to a 1973 study on skin-ridge formation by Hirsch and Schweichel [21], sweat pores are gland secretion ducts opened on the papillary ridges of fingertip surface, at regular intervals (see Fig. 2.3, for an example).

These results were used by Roddy and Stosz [43] to propose a model which is believed to be the unique attempt in literature to explain spatial distribution. In this model, the

[1] There are some reasons to believe that this result is quite general. To take an example, we outline that it can be used to explain outcomes of more recent works [2, 34] reporting that: 1) the average number of sweat pores are significantly less on men's fingers (n.b. that ridge breadth is thinner in women compared to men [36]) and 2) regions of the hand with thicker ridges (e.g., thumb, index finger [36]) have a lower pore density.

pore distribution is assumed to be purely homogeneous and isotropic. In such a case, each pore is a unit of a lattice structure, such that adjacent pores are separated by a fixed distance. Although simple, this approach almost never deals with situations in which two pores appear in close proximity to each other [21, 37, 43]. In order to face these aspects, our approach, unlike the one by Roddy and Stosz [43], avoids making priori assumption on homogeneity and isotropy and, as illustrated in Chapter 5, explores the competitive interaction which exists among the features (pores, in this case) and the minimum-energy path linking them.

2.2 Discussions and Conclusions

In this chapter we examined the related work on fingerprint image quality. As we can see from this review, prior works in literature are generally limited in the sense that they are based mainly on the iconic representation and conditions of the input images. We also reviewed the state of art dedicated to pore spatial distribution which, as mentioned previously, relies upon unrealistic assumptions on the spatial distribution of features. Unlike these previous attempts, we introduced in this thesis a methodology for fingerprint quality analysis which avoids priori assumptions about this type of distribution. The proposed methodology takes into account the spatial interrelationship between the interest features (the pores) and some basic transformations involving point process and anisotropic analysis. The next chapter presents the background necessary to the understanding of our approach.

Chapter 3

Theoretical Foundation

Throughout this work, we restrict attention to mapped data observed through a window $\mathcal{W} \subset \mathbb{R}^d$ (see Figure 3.1, for an example in $\mathbb{R}^2$). In order to give a self-contained understanding of the work, we review some previous theoretical thinking about this kind of data. We start this chapter with a few description notions of mapped data in metric spaces. Next, we present a methodology that can be used to study the degree of regularity of patterns of points having an underlying anisotropic structure, as it is the case for the set of the extracted features considered in this work (the level-3 fingerprint features represented by pores). As we will discuss elsewhere, the observed level of regularity of these features, represented here by sets of points, can reveal possible interactions between these objects and yield the definition of interesting algorithms closely related to fingerprint image quality.

3.1 Point Patterns

From a theoretical perspective, spatial data like the one depicted in Figure 3.1 can be described mathematically as a *finite* and *unordered* set of points [55]

$$\mathcal{S} = \{\mathbf{p}_1, \ldots, \mathbf{p}_n\},\ n \geq 0, \mathbf{p}_i \in \mathcal{W},$$

in some space $\mathcal{X} \subseteq \mathbb{R}^d$, where, obviously, $d \geq 1$ and $\mathcal{W} \subset \mathcal{X}$. The window $\mathcal{W}$ is assumed to have finite positive volume $|\mathcal{W}|$. In the sequel of this thesis, each set $\mathcal{S}$ will be referred to as *configuration*.

In order to give a rigorous measure-theoretical foundation to this description, some authors [11, 12, 55] have imposed a certain structure on the set $\mathcal{X}$. Here, following these results, we assume that $\mathcal{X}$ is equipped with a metric δ such that $(\mathcal{X}, \delta)$ is complete and separable. For instance, $\mathcal{X}$ could be a compact subset of $\mathbb{R}^n$ equipped with the Euclidean distance. This metric defines a topology and a Borel σ-algebra. In the following, a strong condition for $\mathcal{S}$ is sought so that, in any Borel set $A \subseteq \mathcal{X}$, there is at most a finite number of points. In such a case, the sought-after $\mathcal{S}$ is said to be a *locally finite* configuration. The family of all locally finite configurations will be denoted by N^{lf}. With these considerations, a mathematical definition of *point process* can now be recalled [55].

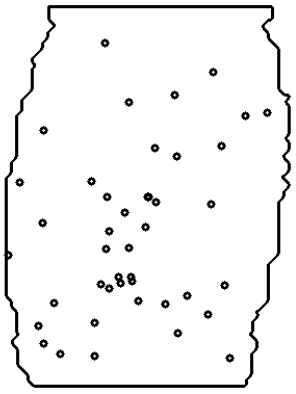

Figure 3.1: Example of spatial observation in $\mathbb{R}^2$. In this work, each point indicates, for example, the location of a minutiae or a pore in a fingerprint image. The window $\mathcal{W}$ from which the features are observed is represented by the silhouette of the whole fingerprint.

Definition 3.1.1 (Point Process) *Let $(\mathcal{X},\ \delta)$ be a complete, separable metric space. A point process on $\mathcal{X}$ is a mapping X from a probability space $[\Omega,\ \mathcal{A},\ \mathbb{P}]$ into N^{lf}, such that for all Borel sets $A \subseteq \mathcal{X}$, the number of points falling in A, $N(A) = N_X(A)$, is a finite random variable.*

In the above definition, the probability space $[\Omega,\ \mathcal{A},\ \mathbb{P}]$ is a mathematical model for a random experiment, where Ω is a set representing the sample space of the experiment, $\mathcal{A}$ is a σ-algebra representing events, and $\mathbb{P} : \mathcal{A} \mapsto [0, 1]$ is a probability measure [35].

Next, we consider an example of a simple and widely used stochastic process.

3.1.1 Poisson Process

The most fundamental and simplest spatial phenomenon is one in which points are distributed uniformly and independently over the space $\mathcal{X}$. We often takes the example of the *complete spatial randomness*, meaning that the events are equally likely to occur anywhere and do not interact with each other. In particular, one can also consider the *non-homogeneous* case where the events are distributed following an intensity function ρ, $\rho : \mathcal{W} \mapsto \mathbb{R}$.

The mathematical model whereby these phenomena can be described is called a *Poisson process*. A Poisson process [55] with intensity function ρ is a process satisfying the following properties:

i) the number of points $N(B)$ in any region B is a Poisson random variable;

ii) the expected number of points in B is given by $\mathbb{E}(N(B)) = \int_B \rho(\mathbf{u})\mathrm{d}\mathbf{u}$;

iii) if B_1 and B_2 are disjoint sets then $N(B_1)$ and $N(B_2)$ are independent random variables, and

iv) if there are n points in a region B then they are distributed independently following a probability density $p(\mathbf{u}) = \frac{\rho(\mathbf{u})}{T}$, where $T = \int_B \rho(\mathbf{u})\mathrm{d}\mathbf{u}$.

It is worth noting that, in homogeneous cases, $\rho(\mathbf{u})$ is constant for all $\mathbf{u} \in \mathcal{X}$.

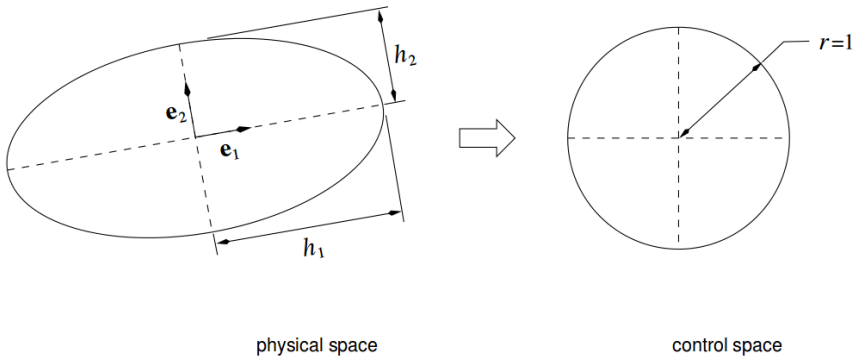

Figure 3.2: Geometric interpretation of metric tensor.

3.2 Anisotropic Analysis

The fingerprint features studied in this work, namely pores and minutia, are good examples of mapped data having an underlying anisotropic structure. This reasoning is twofold: a) the features lie only on the ridges, b) ridges are non-stationary components having distinct directions and widths along the fingers.

To treat anisotropic aspects in a more specific and formal way, we assume that the structural anisotropy of the fingerprint features can be modeled by a metric tensor field $\mathcal{M}$, and the set of interest features can be represented by a configuration of points $\mathcal{S}$ observed through a window $\mathcal{W} \subset \mathcal{X} \subseteq \mathbb{R}^d$. The metric tensor field [14, 29, 31] embeds a certain structure on the space $\mathcal{X}$, in the sense that, at each position $\mathbf{p} \in \mathcal{X}$, there is a positive definitive metric tensor $\mathcal{M}(\mathbf{p})$ which dictates how lengths and angles are measured from the perspective of $\mathbf{p}$. The domain $\mathcal{X}$ and the metric tensor field $\mathcal{M}$ together are a *Riemannian manifold* [7] denoted by $(\mathcal{X}, \mathcal{M})$. Each metric tensor $\mathcal{M}(\mathbf{p})$ is most easily represented as a $d \times d$ symmetric positive-definitive matrix. This matrix can be factored as the product of a rotation matrix $\mathcal{R}$ and a diagonal scaling matrix Γ so that:

$$\begin{aligned} \mathcal{M}(\mathbf{p}) &= \mathcal{R}\Gamma\mathcal{R}^{-1} \\ &= \begin{pmatrix} \vec{e_1} & \vec{e_2} \end{pmatrix} \begin{pmatrix} h_1^{-2} & 0 \\ 0 & h_2^{-2} \end{pmatrix} \begin{pmatrix} \vec{e_1} \\ \vec{e_2} \end{pmatrix}. \end{aligned} \tag{3.1}$$

Visually, as illustrated in Fig. 3.2, each metric tensor $\mathcal{M}(\mathbf{p})$ can be interpreted as a transformation that maps an ellipse to a unit circle. The columns of $\mathcal{R}$ are the eigenvectors of $\mathcal{M}(\mathbf{p})$ concerning the pair of directions: one parallel ($\vec{e_1}$) and the other perpendicular ($\vec{e_2}$) to the flow orientation of the anisotropic process. The diagonal terms of Γ are the eigenvalues of $\mathcal{M}(\mathbf{p})$ indicating the magnitude of the anisotropic forces acting on the process. For a fingerprint, $\mathcal{R}$ and Γ are related to values representing the ridge direction and width, respectively. Note that if the metric tensor field $\mathcal{M}$ is *isotropic* (i.e., for all points the metric tensor remains the identity matrix, or a constant multiple of this matrix), then the structured space $(\mathcal{X}, \mathcal{M})$ corresponds to the standard Euclidean topology.

The resulting structure supplied by the metric tensor $\mathcal{M}$ provides alternatives to the use of conventional metrics (e.g., Euclidean distance, city block distance) in the distance

computation between any two points in $\mathcal{X}$ [7, 31]. Particularly, we reuse the definition of directional distance function in [14] as follows.

Definition 3.2.1 (Directional Distance) *Let* $\mathbf{p}$ *and* $\mathbf{q}$ *be two points in* $\mathcal{W}$*, and* $\mathcal{M}(\mathbf{p})$ *be a metric tensor. The directional distance* $\delta_{\mathbf{p}}$ *is defined by:*

$$\delta_{\mathbf{p}}(\mathbf{p}, \mathbf{q}) = \sqrt{\overrightarrow{\mathbf{pq}}^t \mathcal{M}(\mathbf{p}) \overrightarrow{\mathbf{pq}}}, \tag{3.2}$$

where $\overrightarrow{\mathbf{pq}}$ *denotes the vector pointing from* $\mathbf{p}$ *to* $\mathbf{q}$*.*

The above function computes the distance between two points, $\mathbf{p}$ and $\mathbf{q}$, but only w.r.t. the first one. In this sense, it can be interpreted as a simplification of the classical Riemannian distance which considers the whole path connecting two points and measures the distance from $\mathbf{p}$ to $\mathbf{q}$ through smooth steps. Also, one can observe that, unlike the usual metrics (e.g., Euclidean distance), the directional distance is not always symmetric.

Next, we use the above notions to present an extension to the classical *Voronoi Diagram*. A Voronoi diagram is a partition of the space from which a given configuration is defined into convex polygons, also known as *Voronoi regions*. The following definition [14] generalizes this diagram and introduces its anisotropic counterpart.

Definition 3.2.2 (Anisotropic Voronoi Diagram) *Given a structured space* $(\mathcal{X}, \mathcal{M})$ *and a configuration* $\mathcal{S} = \{\mathbf{p}_1, \ldots, \mathbf{p}_n\}$ *observed in a window* $\mathcal{W} \subset \mathcal{X}$*, the set* $\{\mathcal{V}_i\}_{i=1}^n$ *is called a diagram of* $\mathcal{W}$*, with respect to* $(\mathcal{X}, \mathcal{M})$ *and* $\mathcal{S}$*, if* $\mathcal{V}_i \cap \mathcal{V}_j = \emptyset$*, for* $i \neq j$ *and* $\cup_{i=1}^n \mathcal{V}_i = \mathcal{W}$*. The Voronoi region* $\mathcal{V}_i$ *corresponding to the point* $\mathbf{p}_i$ *is given by:*

$$\mathcal{V}_i = \{\mathbf{y} \in \mathcal{W} \mid \delta_{\mathbf{y}}(\mathbf{y}, \mathbf{p}_i) \leq \delta_{\mathbf{y}}(\mathbf{y}, \mathbf{p}_j), \text{ for all } i \neq j\}. \tag{3.3}$$

Points having equal directional distances to any two configuration's points $\mathbf{p}_i$*,* $\mathbf{p}_j$ *are called their bisectors.*

Fig. 3.3 illustrates this anisotropic definition under distinct metric tensor fields, where black circles in the diagram (four points at the corners plus one central point) indicate the location of the configuration points in $\mathcal{S}$. Diagrams for isotropic and anisotropic scenarios are illustrated in Fig. 3.3a and 3.3b, respectively. As we can observe, in both cases, the above anisotropic definition results in diagrams taking the usual shape: each Voronoi region $\mathcal{V}_i$ of a configuration point $\mathbf{p}_i$ is the set of all points in the manifold that are at least as close to $\mathbf{p}_i$ as to any other point. So if $\mathcal{M}$ is isotropic, the anisotropic diagram is the classical Voronoi diagram (Fig. 3.3a). Since the above generalization carries a significant amount of freedom, it is not surprising that there conveys at least an important distinction. While the dual of the standard Voronoi diagram is the *Delaunay triangulation*, the anisotropic diagram can be very complicated and its geometric dual may contain irregularities that not always lead to an embedded triangulation. From [4], we have that if a configuration produces *orphan-free* anisotropic Voronoi diagram, using the above definition, then its dual is always an embedded triangulation. A diagram is orphan-free if its regions $\mathcal{V}_i$ are connected, for all i, $1 \leq i \leq n$ (equivalently, each cell, or connected component of a Voronoi region, contains its generating site).

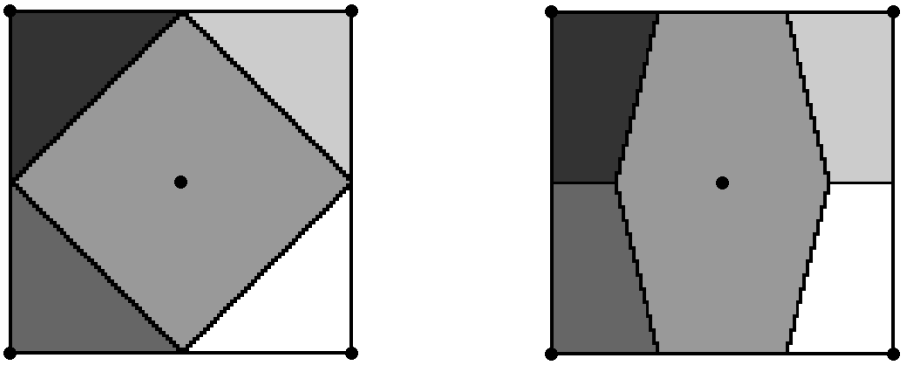

(a) Diagram defined w.r.t. a uniform tensor field $\mathcal{M}$, where $\mathcal{M}(\mathbf{p}) = \left(\begin{smallmatrix} 1 & 0 \\ 0 & 1 \end{smallmatrix}\right)$, $\forall \mathbf{p} \in \mathcal{W}$.

(b) Diagram defined w.r.t. a uniform tensor field $\mathcal{M}$, where $\mathcal{M}(\mathbf{p}) = \left(\begin{smallmatrix} 1 & 0 \\ 0 & 4 \end{smallmatrix}\right)$, $\forall \mathbf{p} \in \mathcal{W}$.

Figure 3.3: Anisotropic Voronoi Diagrams.

Focusing mainly on a spatially distributed configuration of points, we highlight two important structural properties of the Voronoi partition which will be explored in this work. We start by assuming an orphan-free diagram to keep the link between an anisotropic Voronoi diagram and its corresponding triangulation. The first property concerns the *empty circum-ellipse* definition enunciated in [4] which states that there is some ellipse that circumscribes sites corresponding to $\mathbf{p}_1, \mathbf{p}_2, \ldots \mathbf{p}_k$ and containing no other point in its interior. This implies that inserting or removing a new point in the configuration will affect only the Voronoi regions whose circum-ellipses contain that point. The other property, very useful here, concerns the fact that for an optimal configuration of points, with very regular distribution, each point $\mathbf{p}_i$ coincides with the centroid location of the corresponding Voronoi region $\mathcal{V}_i$. This optimal configuration is known as the *anisotropic centroidal Voronoi diagram* [13, 14]. Fig. 3.4 shows an example of the Voronoi diagram for two configurations of points represented by black circles. The corresponding centroid positions are indicated by red $\times$'s. As we can observe from the images, arbitrary chosen points (Fig. 3.4a) do not correspond to the centroids of their associated Voronoi regions. On the other hand, in the optimal configuration case (Fig. 3.4b), we have each point coinciding with its centroid position.

In practice, the above property related to the *empty circum-ellipse* definition implies that missing or spurious features would affect the Voronoi diagram only locally. As we will illustrate in the next chapter, this result, associated with the optimal configuration of points, suggests an interesting way to study the regularity level of the spatially distributed sets of points represented by our interest features.

3.3 Discussions and Conclusions

This chapter considered some notions on mapped data observed through a window $\mathcal{W} \subset \mathbb{R}^d$. Further, we described a methodology to study patterns of points having an underlying anisotropic structure, as it is the case for the set of extracted features considered in this work (level-3 fingerprint features represented by pores). In Chapter 5, we will illustrate

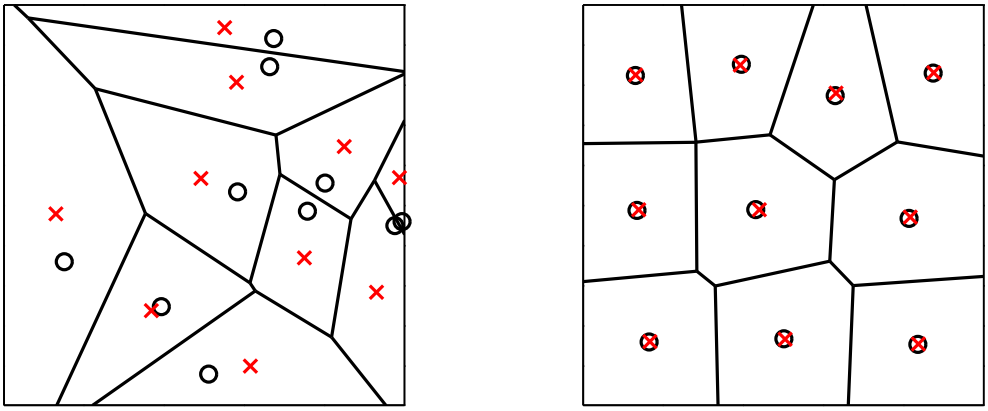

(a) (b)

Figure 3.4: Example of random and very regular configurations of points.

how these concepts can be integrated to approach the problem of fingerprint quality assessment. Before that, we will introduce, in the next chapter, a new framework for fingerprint quality analysis which takes into account the spatial interrelationship between the corresponding interest features.

Chapter 4

Proposed Framework

The comparison of two fingerprints by an AFIS involves basically the set of features extracted from the fingerprint images and the real value defining a similarity score. Since high-quality fingerprints consisting mainly of reliable features might lead to a more precise matching, it is natural to ask if a quality index should be computed directly from a set of extracted features. That is the question we attempt to answer in this chapter. To do so, we introduce a methodology aiming at a stronger theoretical ground for this feature-based quality analysis.

4.1 Problem Statement

Given a configuration $\mathcal{S}$ observed through a window $\mathcal{W} \subset \mathbb{R}^2$ (see Chapter 3) concerning the locations of a set of features extracted from a gray-scale fingerprint image $\mathcal{I}$, $\mathcal{I} : \mathbb{Z}^2 \mapsto \mathbb{Z}$, our goal is to assess the quality of subsets of $\mathcal{S}$ as well as of any given region in $\mathcal{W}$. To this end, we begin with the intuition that, for any previous defined window $\mathcal{W}$, some biological mechanisms involving the fingerprint formation, together with some physical phenomena related to the image acquisition, impose certain arrangements on both set $\mathcal{S}$ and image $\mathcal{I}$. Thus, the quality problem becomes one of modeling the mechanisms related to the way the arrangements of features arise.

In this respect, we propose a conceptual framework whereby new quality assessment algorithms will be built by taking into account the following groups of analysis:

1. *Spatial*: The quality algorithms in this group are based on reflections about arrangements of features of the same type (e.g., pores and pores, minutia and minutia). The central question is the following: are the features locations in $\mathcal{S}$ plausible? With this applied goal in mind, we will take advantage of the clustering tendency of the minutia [63] or the regularity of the fingerprint sweat pores [43].

2. *Structural*: Algorithms that fall in this category are based on properties about arrangements of features of different types (e.g., pores and local fingerprint phase, pores and local orientation field, minutiae and singular points). Now, the central question is: is the set $\mathcal{S}$ coherent with other available information drawn from image $\mathcal{I}$? For example, by exploring the fact that there exist a higher minutiae density in

regions containing singular points [8] such as cores and deltas, we can somehow use the positions of these singular points to verify whether some regions containing a set $\mathcal{S}$ of minutia present a proper feature distribution.

The potential of the above formulation will be demonstrated in Chapter 5 by focusing on fingerprint pores (level-three features). To the best of our knowledge, this is the first work that explores such a kind of approach for quality assessment purpose.

4.2 Degradation Models

At this point, it is of paramount importance to recall some uncontrolled factors that can affect the processing of the fingerprint images. In one respect, we remember the role played by the different skin conditions (e.g., dryness, humidity), residues from previous captures and inconsistent contact. In another respect, it is worthy noting that the algorithms used for image preprocessing, segmentation, and feature extraction are generally imperfect and often introduce measurement errors. The quality of a given input set of features relies on one or more of these situations resulting in a wide spectrum of behaviors, ranging from the ideal case, which comprises error-free feature sets, to the other extreme which consists of a set that is either empty or full of spurious features. In order to cope with the so many situations lying in-between these two extremes, we design an error model based on multiple spatial phenomena. As we will see, the premise underlying this approach is twofold, namely, we assume that 1) the biological mechanisms generating reliable configurations can be seen as a point process, and 2) the errors affecting a given reliable configuration $\mathcal{S}$ can be modeled by a certain spatial transformation. In such a case, distinct error regions can be modeled by applying some useful transformations to $\mathcal{S}$ (e.g., thinning, superposition, mapping, and random displacement [55]).

Given a regional subset $\mathcal{E} \subset \mathcal{W}$ of the window in which a configuration $\mathcal{S}$ is observed, the transformations considered in this work and directly involved with $\mathcal{E}$ can be grouped into the following categories:

1. *Regional randomness*: The operation describing the *regional randomness* can simply be defined as a realization of a Poisson process (Section 3.1.1) in $\mathcal{E}$. Here we are obviously treating cases where errors are i.i.d. in $\mathcal{E}$ and related to the intensity function ρ.

2. *Intra-ridge randomness*: An alternative to the i.i.d. assumption is to consider a non-homogeneous model whereby the errors are distributed w.r.t. a Poisson process defined only on fingerprint ridges.

3. *Random superposition*: Let $\mathcal{S}_i$ and $\mathcal{S}_r$ denote, respectively, an error-free feature set and a configuration generated through the regional randomness transformation given before. Then, the transformation associated with the *random superposition* corresponds simply to the union between $\mathcal{S}_i$ and $\mathcal{S}_r$.

4. *Intra-ridge random superposition*: The transformation involved in the *intra-ridge random superposition* corresponds to the union between $\mathcal{S}_i$ and $\mathcal{S}_c$, where, again, $\mathcal{S}_i$

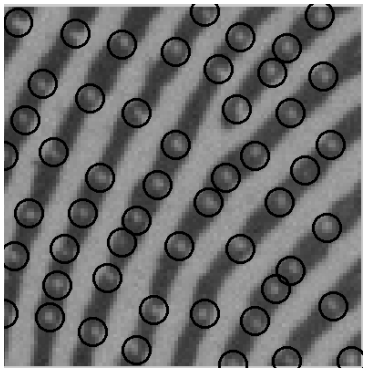

(a) Error-free configuration $\mathcal{S}$ superimposed on an image block.

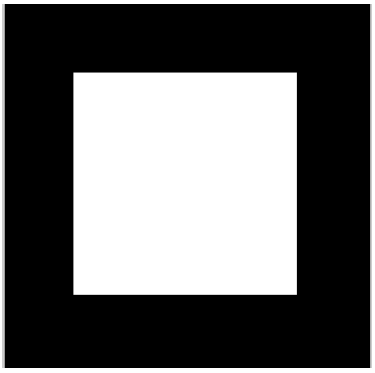

(b) Image mask representing the subset $\mathcal{E}$.

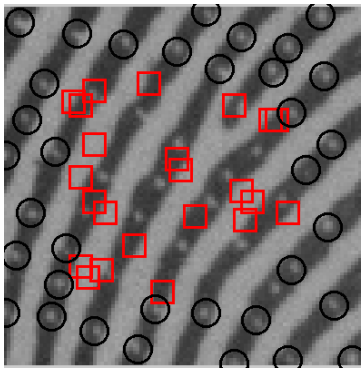

(c) Regional randomness configuration superimposed on the image block (a).

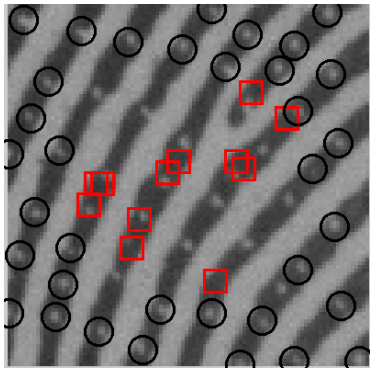

(d) Intra-ridge randomness configuration superimposed on the image block (a).

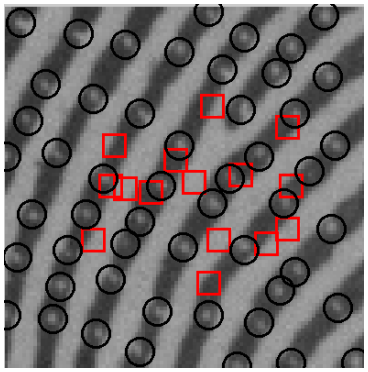

(e) Random superpostion configuration superimposed on the image block (a).

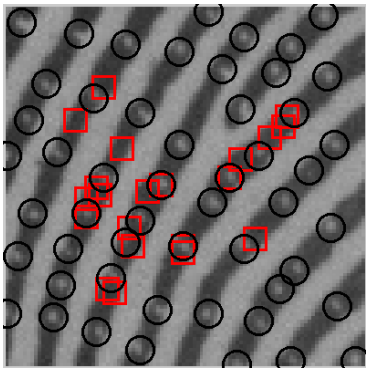

(f) Intra-ridge random superpostion configuration superimposed on the image block (a).

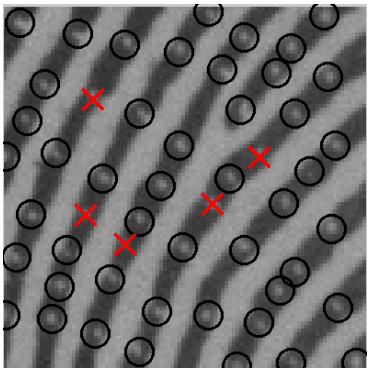

(g) Thinning configuration superimposed on the image block (a) with probablity $p = 0.3$.

Figure 4.1: Illustration of the errors according to the proposed error models.

indicates an error-free configuration and $\mathcal{S}_c$ is a configuration describing an intra-ridge randomness. The rationale behind this superposition operation relies on cases where the algorithms associated with feature extraction can identify positive results properly but fail to recognize some false features. The intensity function ρ is closely related to the *specificity* of this extraction.

5. *Random thinning*: The thinning transformation consists of using some predefined rule to remove points from a configuration $\mathcal{S}$ to form a new set $\mathcal{S}_t$. In this work, we use the following simple rule: each point of $\mathcal{S}$ is independently removed (or kept) with some probability p (or $1-p$). In such a case, we treat situations where the algorithms involved in the feature extraction lack ability to precisely identify positive results. The *sensitivity* of this filtering is driven by the probability p.

The above models are illustrated in Fig. 4.1 for an image block and configuration $\mathcal{S}$ represented by black circles which shows the corresponding set of pores in the ground-truth (Fig. 4.1a). The new pores obtained from each error model are indicated by red squares, except for the case of thinning (Fig. 4.1g), where the removed pores are marked with red $\times$'s.

4.3 Discussions and Conclusions

The central premise of this work is that the quality of a fingerprint sample may be computed directly from a set of extracted features. By exploring spatial and structural properties of the fingerprint features distribution, this chapter introduced a new framework whose design was based on he following questions: (i) are the locations of the extracted features plausible? and (ii) is the set of extracted features coherent with other available information drawn from the captured image? In the next chapter, based on these issues, we will define two quality index algorithms for the case of level-3 fingerprint features represented by pores. Furthermore, we also present in this chapter some point process transformations that can be used to model feature configurations with distinct specificity and sensitivity levels. These transformations will be explored in Chapter 6 in the development of a new fingerprint quality dataset.

Chapter 5

Feature-based Quality Algorithms

From the previous discussion, we can state that the problem of feature-based quality assessment can be seen as a quantification problem where certain arrangements of an input set of features have to be evaluated according to some statistical models related to the way the interest features arise. The key point of this process is to find a set of discriminant models allowing the construction of appropriate algorithms. In this chapter, we propose novel algorithms which, together with the corresponding models, illustrate the main ideas discussed in Chapter 4.

5.1 Spatial Algorithm

The first algorithm considers the spatial distribution of the fingertip sweat pores. Shortly, this analysis consists of a) definition of the region of influence associated with each feature location and b) evaluation of the relative position of the centroids for each obtained region. As explained next, the reasoning for such a procedure is closely related to the way the pores arise along the ridges.

To understand why the pores location lies at areas surrounding the centroid coordinates, it is important to recall the well-known *regularity* of the fingerprint pores. As stated, for instance, in the work by Roddy and Stosz [43], the sweat pores are spread at regular intervals in the papillary ridges. This information, combined with some biological evidences (e.g., stabilization forces by acting when sweat gland secretion ducts open on to the fingertip surface) about this fact reported in [21] and [39], led us to propose a new quality index model taking into account the competitive interactions among the pores coordinates. Since these interactions may make it unlikely, but not impossible, that two pores can appear in close proximity to each other, we address the question concerning the way these pores arise from an energy-optimization standpoint. In this regard, we assume that the biological mechanisms involved in the process can be described in terms of the centroidal Voronoi Diagram paradigm [13], where an optimal configuration consists of points that coincide with the centroids of the corresponding Voronoi regions. To our knowledge, this is the first attempt to model the mechanism regarding the spatial interaction of the fingerprint sweat pores.

Based on this assumption, we propose the following global quality algorithm. Let

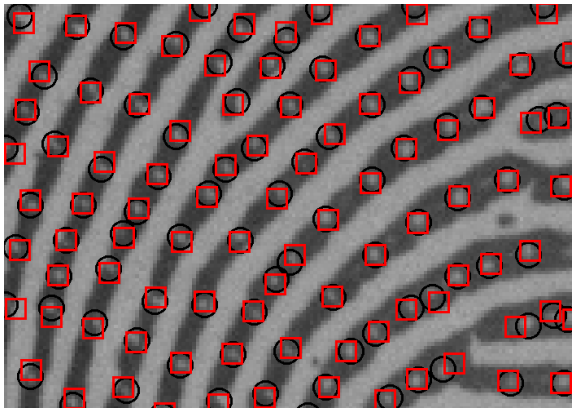

Figure 5.1: Comparison between a real and modeled pores distribution considering an energy-optimization standpoint. Black circles represent the features in the ground-truth.

$\mathcal{S}$ be a configuration related to the positions of a given set of pores extracted from a high-resolution fingerprint image $\mathcal{I}$. Our spatial algorithm consists mainly of three steps:

1. Compute the classical Voronoi Diagram for the configuration $\mathcal{S}$. From now on, each individual region obtained from a point $\mathbf{p}_i$ of the configuration will be denoted by $\mathcal{V}_i$, so that the resulting diagram is indicated by $\{\mathcal{V}_i\}_{i=1}^{n}$.

2. Compute the centroid $\mathbf{c}_i$ for each Voronoi region $\mathcal{V}_i$.

3. Evaluate the quality of the configuration $\mathcal{S}$, by taking into account the observed value d_i, $d_i = \|\overrightarrow{\mathbf{p}_i\mathbf{c}_i}\|$, i.e., by measuring the distance from a given feature location $\mathbf{p}_i$ ($\mathbf{p}_i \in \mathcal{S}_j$) to the corresponding centroid $\mathbf{c}_i$. Particularly, we explore the fact that the majority of the pores location lies within a certain range to the corresponding centroids (see Fig. 5.1). In this respect, we analyze the distribution of the distances d_i for all points in $\mathcal{S}$. The global quality index $\mathcal{Q}_1(\mathcal{S})$ is given by:

$$\mathcal{Q}_1(\mathcal{S}) = \sum_{p_i \in \mathcal{S}} 1\{d_i \geq \text{rng}\}. \tag{5.1}$$

   In terms of implementation issues, the value concerning the distance range, rng, in Eq. 5.1 can be set up by analysing some distances between the feature-location and the corresponding centroid coordinates obtained from a representative set of distinct images. In this work, we set experimentally rng = 5. Naturally, the less the $\mathcal{Q}_1$ value, the higher the image quality.

Fig. 5.1 shows a comparison between a real and modeled spatial distribution of a set of pores. In this figure, the centroids of the corresponding Voronoi regions are represented by red squares, whereas the original feature positions, defined in the ground-truth (see Section 6.1), are indicated by black circles. As we can see, each pore does lie very close to the corresponding centroid position.

The above quality information is illustrated in Fig. 5.2 for a set of features with different quality levels. Fig. 5.2a shows a high-quality configuration of pores superimposed on a fingerprint image. In such an ideal case, the majority of the pores remains very close

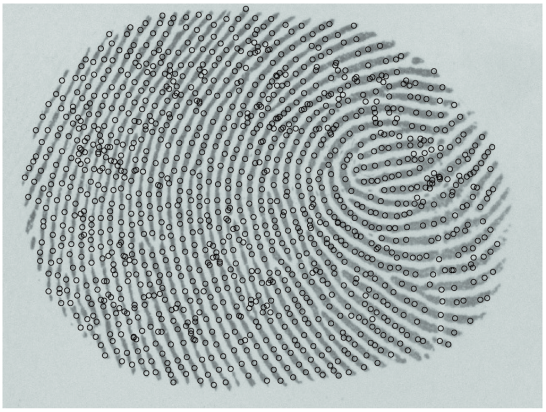

(a) High-quality configuration $\mathcal{S}$ with $\mathcal{Q}_1 = 3$ superimposed on a fingerprint image.

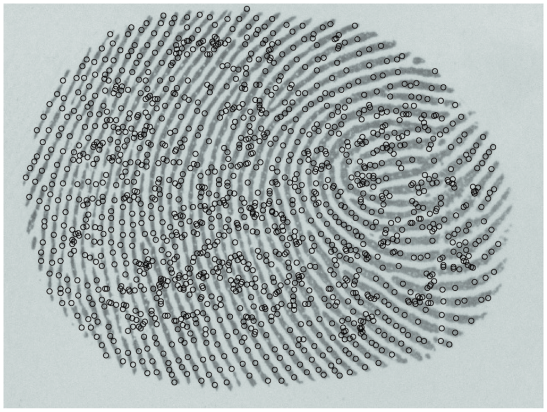

(b) Low-quality configuration $\mathcal{S}$ with $\mathcal{Q}_1 = 46$ superimposed on a fingerprint image.

Figure 5.2: Illustration of the global quality index $\mathcal{Q}_1$.

to the corresponding centroids, thus defining a high quality configuration index ($\mathcal{Q}_1 = 3$). Fig. 5.2b shows an example of a low-quality configuration ($\mathcal{Q}_1 = 46$) in which the pores do not lie close to the corresponding centroid positions (due to capture errors, for example).

5.2 Structural Algorithm

Another way to explore the relationship among pores locations is to consider that the fingerprint ridges do arise along a minimum energy path linking distinct pores. In this sense, we can define an algorithm for fingerprint quality analysis, concerned with the structural content of the images, by considering more directly the energy propagation yielded by the optimization mechanism characterizing the competitive interaction between sweat pores (Section 5.1). As we will show next, this algorithm takes into account the anisotropic framework stated in Section 3.2. Beforehand, we consider the *Voronoi-energy map* as the resulting energy map defined along the space from which the features are observed.

Definition 5.2.1 (Voronoi-energy map) *Given a structured space $(\mathcal{X}, \mathcal{M})$ and a configuration $\mathcal{S} = \{\mathbf{p}_1, \ldots, \mathbf{p}_n\}$ observed in a window $\mathcal{W} \subset \mathcal{X}$, the Voronoi-energy map, $E : \mathcal{W} \mapsto \mathbb{R}$, is defined at each location $\mathbf{y}$, $\mathbf{y} \in \mathcal{W}$, as:*

$$E(\mathbf{y}) = \min\{\delta_{\mathbf{y}}(\mathbf{y}, \mathbf{p}_k)\}, \text{for all } \mathbf{p}_k \in S. \tag{5.2}$$

Informally, for each point $\mathbf{y}$ in the observation domain $\mathcal{W}$, the above defined map assigns a value measuring the shortest directional distance stated in Section 3.2, $\delta_{\mathbf{y}}$, from $\mathbf{y}$ to the closest configuration point in $\mathcal{S}$. In this sense, the resulting mapping describes the energy propagation underlying the Anisotropic Voronoi Diagram defined w.r.t. $\mathcal{S}$ (see Section 3.2). Fig. 5.3 illustrates the Voronoi-energy map for a high-resolution fingerprint fragment (Fig. 5.3a). The Voronoi-energy map E is depicted in Fig. 5.3b where the pixels

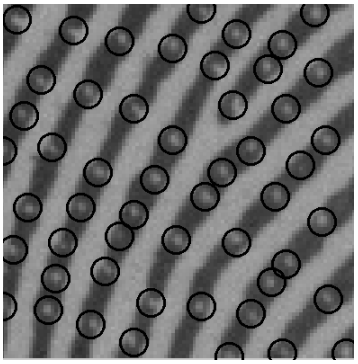

(a) Error-free configuration $\mathcal{S}$ superimposed on an image fragment.

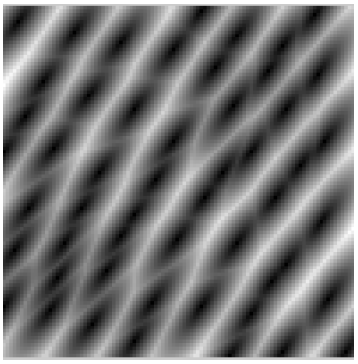

(b) Voronoi-energy map E w.r.t. the configuration in (a).

Figure 5.3: Illustration of the Voronoi-energy map.

value, given by Eq. 5.2, ranges form black to white and indicate, respectively, the lowest and highest energy. Notice that the paths depicted in Fig. 5.3b linking distinct pores upon a minimum-energy trajectory are consonant with the respective ridges in the fingerprint fragment (Fig. 5.3a).

The next quality index uses the notion of minimum-energy propagation to reconstruct a representation of the fingerprint phase based on the available features. The quality information will be given by the 2D-correlation between this reconstructed phase and the corresponding one extracted from the input image. As illustrated in Fig. 5.4, the main steps of this structural algorithm are as follows:

1. Construct a metric tensor field $\mathcal{M}$ for the configuration $\mathcal{S}$, by taking into account the anisotropic information of the ridges of an image $\mathcal{I}$. The direction of the ridge components can be easily obtained from the gradients in $\mathcal{I}$ [22].

2. Consider Definition 5.2.1 to estimate the Voronoi-energy map E for the points in $\mathcal{S}$ w.r.t. the metric tensor field $\mathcal{M}$. In such a case, the observation window $\mathcal{W}$ (the region of interest) can be defined by the *convex hull* of the points in $\mathcal{S}$.

3. To reconstruct the phase image, $P_{\mathcal{S}}$, from the set of features in $\mathcal{S}$, highlight the minimum-energy path information in the above Voronoi-energy map E. This local enhancement is given here by a Gabor filtering which uses the local directions and frequencies of the ridges estimated from E [22]. Throughout this thesis and following the works in [6, 15, 44], the term reconstruction is used to indicate the regeneration of fingerprints from the stored feature coordinates.

4. Estimate the phase image, $P_{\mathcal{I}}$, from the input image $\mathcal{I}$, by applying, once again, the previous enhancement operation directly to $\mathcal{I}$.

5. Divide $P_{\mathcal{S}}$ into non-overlapping blocks, $\mathcal{F}_j$, of size $w \times w$. For the 1200 dpi image resolution considered in this work, we set experimentally $w = 40$.

6. Apply the previous splitting operation to the estimated phase $P_{\mathcal{I}}$ so that $\mathcal{H}_j$ indicates an image block of size 40×40 of $P_{\mathcal{I}}$.

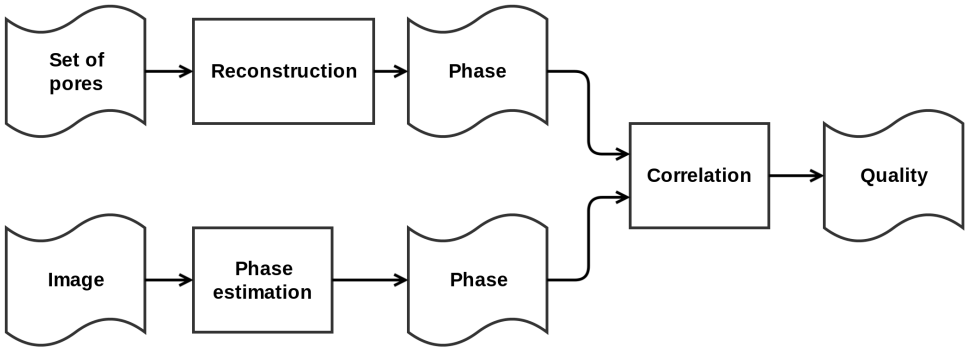

Figure 5.4: Flowchart of structural algorithm.

7. Evaluate the quality of each image block $\mathcal{F}_j$, by computing the 2D-correlation between the estimated phase image $P_{\mathcal{S}}$ and the corresponding information $P_{\mathcal{I}}$ for each image block, as follows:

$$\mathcal{Q}_2(\mathcal{F}_j) = \text{corr}(\text{z-score}(\mathcal{F}_j),\ \text{z-score}(\mathcal{H}_j)), \tag{5.3}$$

where corr corresponds to the 2D Pearson's correlation coefficient between the informations contained from the image blocks. The operator z-score indicates the statistical standard score normalization such that the values of a given block are centered and scaled to have, respectively, mean 0 and standard deviation 1. In that way, we can observe that values given by Eq. 5.3 ranges from 0 to 1 and indicate, respectively, lowest and highest quality. High values are associated with high-quality samples of both image $\mathcal{I}$ and set $\mathcal{S}$.

Fig. 5.5 illustrates, for an ideal case consisting of a configuration $\mathcal{S}$ representing the ground-truth, the above phase reconstruction for a high-resolution fingerprint image (Fig. 5.5a). The corresponding Voronoi-energy map is depicted in Fig. 5.5b. The white regions in Fig. 5.5b indicate points lying outside of the fingerprint window $\mathcal{W}$ (the convex-hull defined by the set of features). Fig. 5.5c shows the estimated phase $P_{\mathcal{I}}$ of the input image $\mathcal{I}$. The reconstructed phase estimated from the pores coordinates extracted from $\mathcal{I}$ is depicted in Fig. 5.5c. As we can see from this example, in such an ideal case, there is an evident visual correspondence between the estimated phase images $P_{\mathcal{I}}$ (Fig. 5.5c) and $P_{\mathcal{S}}$ (Fig. 5.5d).

The structural quality map $\mathcal{Q}_2$ is illustrated in Fig. 5.6 for both configurations depicted in Fig 5.2. Fig. 5.6 shows, according to Eq. 5.3, the quality values varying from black to white and corresponding, respectively, to the lowest and highest quality. The block-wise quality computed by considering the configuration in Fig. 5.2a is depicted in Fig. 5.6a. Fig. 5.6b shows the block-wise quality computed by taking into account the configuration in Fig. 5.2b. As we can see, the quality values concerning blocks in the high-quality sample (Fig. 5.6a) are distinguisable to the ones obtained in the low-quality configuration (Fig. 5.6b). The mean quality value obtained in these situations are, respectively, 0.8404

(a) Original input image $\mathcal{I}$.

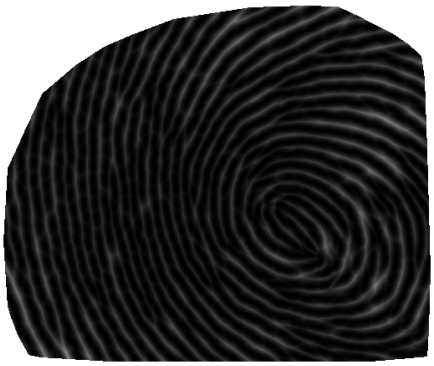

(b) Voronoi-energy map E estimated from the pores in configuration $\mathcal{S}$ comprising the ground-truth obtained from $\mathcal{I}$.

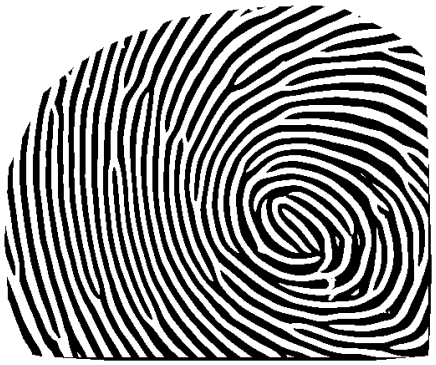

(c) Phase image $P_{\mathcal{I}}$ estimated from the input image $\mathcal{I}$ (Fig. 5.5a).

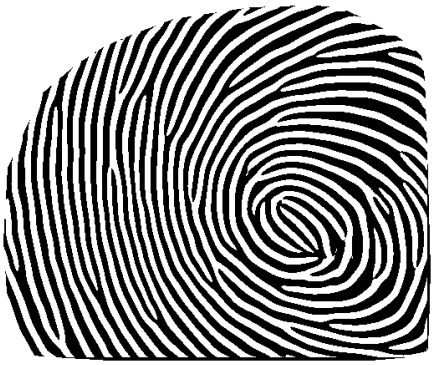

(d) Phase image $P_{\mathcal{S}}$ corresponding to the reconstruction of the fingerprint from the pores coordinates in $\mathcal{S}$.

Figure 5.5: Illustration of the phase reconstruction for an ideal case.

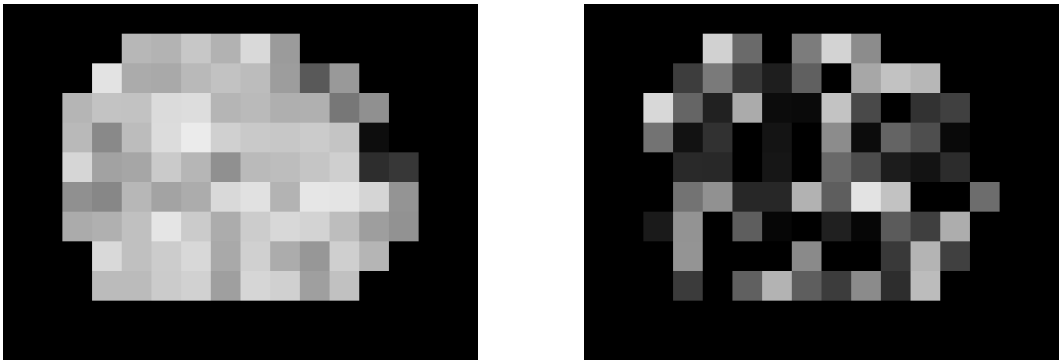

(a) Block-wise quality $\mathcal{Q}_2$ computed by considering the configuration in Fig. 5.2a.

(b) Block-wise quality $\mathcal{Q}_2$ computed by considering the configuration in Fig. 5.2b.

Figure 5.6: Illustration of the structural quality algorithm.

(Fig. 5.6a) and 0.3973 (Fig. 5.6b).

5.3 Discussions and Conclusions

In this chapter we continued the work on feature-based quality assessment started in Chapter 4 and proposed two new quality index algorithms with the focus on fingerprint pores and under an energy-optimization standpoint. The first algorithm explored the fact that, as shown in Section 5.1, the pores location lies at areas surrounding the centroids of Voronoi regions defined w.r.t. the original pores position. The second algorithm (Section 5.2) considered that fingerprint ridges do arise along a minimum energy path linking distinct pores. As we saw here, this contribution relies on models taking into account the way sweat pores arise on fingertips. From this point of view, we can observe that the first algorithm has an underpinning model for the mechanism regarding the spatial interaction among pores location. The second algorithm introduced a method for reconstructing the phase images from a given set of pores coordinates. The next chapter shows the protocol considered in the validation of these contributions and the corresponding experimental results.

Chapter 6

Experiments and Discussions

In this chapter, we carry out three different experiments to illustrate the main results of our approach. In Section 6.2, we assess the introduced spatial and structural models for a consistent set of real fingerprint images. Further, in Section 6.3, we assess the capacity of the proposed structural algorithm to identify low-quality image regions in configurations with distinct error intensities. Finally, since the practical value of a given system depends on its capacity to correctly accept or reject the identity of an individual, we will show in Section 6.4 how the proposed feature-based quality information can be used to improve the identification accuracy. Before proceeding, we introduce a new fingerprint quality dataset constructed according to the error models introduced in Section 4.2. This dataset will be further used in our experiments.

6.1 Dataset

To objectively assess the performance of our approach, we need a dataset of features configuration conveying different levels of quality. In the absence of such a dataset in the biometric community, we extend the well-known PolyU High-Resolution Fingerprint Database [62], in the construction of this required dataset, by considering the set of error models introduced in Section 4.2. The PolyU HRF database consists of $1,480$ fingerprint images of size 640×480, collected in two sessions, from 148 fingers. In each session, separated by two weeks apart, five images of each finger were captured by using a custom built high-resolution sensor with $1,200$ dpi.

To extend the original database, a set of 120 fingerprint images was manually annotated in order to determine the ground-truth. Table 6.1 shows some details of this ground-truth consisting of four different images from 30 fingers and comprising a total of $138,643$ annotated pores location. Further, we combine the 90 images from the first session with the error models in Section 4.2 to give shape to distinct degradation scenarios and model the various problems affecting the set of features. Images from the second session are used as templates for matching (Section 6.4) and are not taken into account here.

The different degradation scenarios of the dataset are obtained by varying the specificity and sensitivity levels associated with the point process transformations described

Table 6.1: A Summary of the ground-truth.

PolyU HRF Collection Session	# Images	# Fingers	# Pores
1	90	30	103,490
2	30	30	35,153
Total	120	30	138,643

in Section 4.2, and acting on a given subset $\mathcal{E} \subset \mathcal{W}$ of a configuration of points. To enrich the error modeling process by randomly considering different subsets, we introduce an error intensity parameter, e, related to the probability of a block-wise foreground region is independently marked. Obviously, the greater this error intensity, the greater the probability of an image block to be marked. These marked blocks are used to define the regional subset $\mathcal{E} \subset \mathcal{W}$ where the corresponding error models are applied.

To improve our analysis, we also separate random and intra-ridge degradations into two distinct datasets, namely DB1 and DB2. For each error intensity ranging in the values 0.4, 0.6 and 0.8, we generate 15 scenarios for each database by taking into account the ratio of specificity and/or sensitivity (including the combination of both) varying in the values 0.2, 0.4, 0.6, 0.8 and 0.9, as illustrated in Table 6.2. More specifically, in the case of intra-ridge degradations, scenarios with different levels of specificity, sensitivity and the combination of both are obtained by applying to the given ground-truth transformations of *intra-ridge random superposition*, *random thinning* and *random thinning* followed by *intra-ridge random superposition*. In the case of random degradations, we consider *random superposition*, *random thinning* and *random thinning* followed by *random superposition*.

Fig. 6.1 shows some configuration examples of features with error intensities equal to 0.4, 0.6 and 0.8. Fig. 6.1a, 6.1b and 6.1b show some image masks representing the randomly marked blocks affected by error transformations. The corresponding configurations are depicted, respectively, in Fig. 6.1d, 6.1e and 6.1f, where the black circles indicate the features position.

At the end of this process, each dataset consists of 4,050 images grouped into 45 scenarios. To our knowledge, this extended set consisting of 9,100 configurations and presenting different levels of specificity, sensitivity, and error intensity is the unique feature-based quality fingerprint dataset currently available [1].

6.2 Validation Issues

The objective of this first experiment is to assess the hypothesis underlying our spatial algorithm (Eq. 5.1) which states that the mechanisms (the competitive interactions) involved in the pores distribution can be described in terms of the centroidal Voronoi Diagram tessellation. In the same way, we also analyze the effectiveness of the reconstruction step associated with our structural approach (Eq. 5.3).

[1] The ground-truth and the extended datasets are available in `https://github.com/raoniteixeira/HRFQDB_UFMT_2015`.

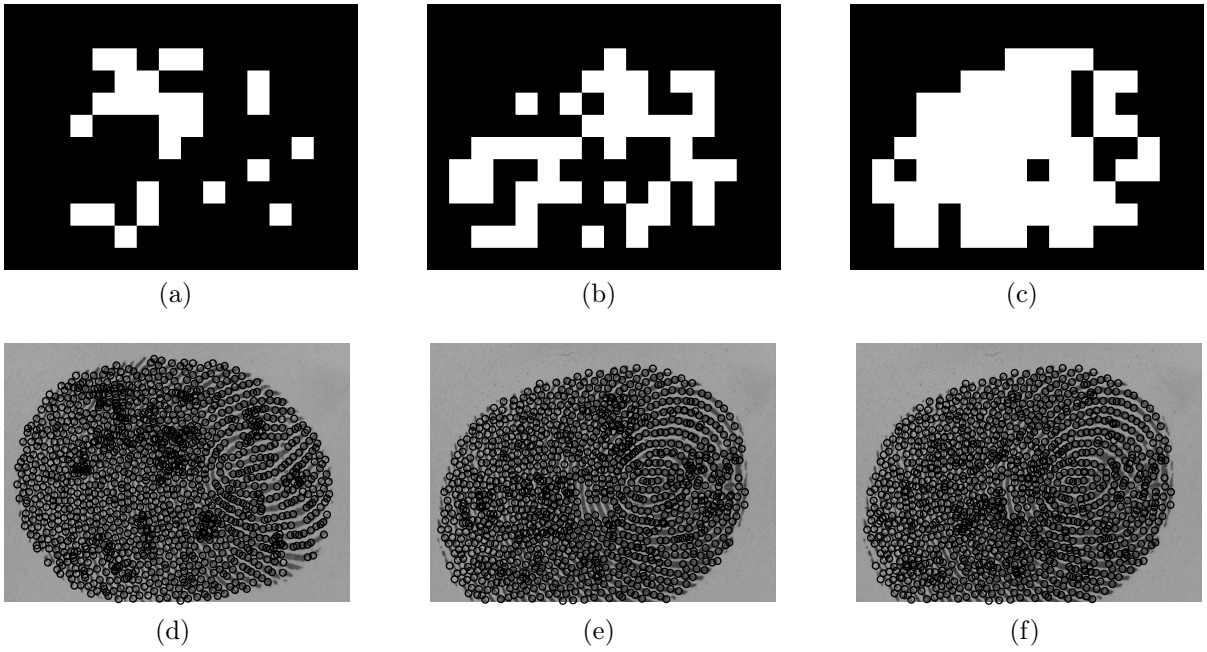

Figure 6.1: Some configurations examples: (a-c) Image masks representing the blocks affected by error transformations, and (d-f) the corresponding configurations superimposed on the respective images.

Fig. 6.2 shows the histogram of the distance between the pores location and the corresponding centroids of the Voronoi regions defined by these pores, for all images in the ground-truth (total of 138,643 pores), indicating that our initial hypothesis can be endorsed. Notice that the majority of the pores analyzed in this experiment (about 86% of the total) lies in a distance inferior to 2 pixels of the corresponding centroid coordinates.

In the second part of this experiment, we analyze the reconstruction of the fingerprint phases encompassed by our structural algorithm. As illustrated by some examples in Fig. 6.3, a visual analysis of the fingerprint images reveals that the phase image defined by our approach is fairly consistent with the ridges structures present in the input images. As we can see in Fig. 6.3, unlike some previous attempts based on level-2 fea-

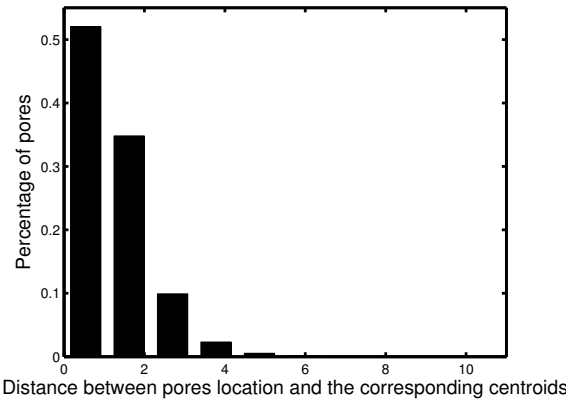

Figure 6.2: Histogram of the distances between the pores location and the corresponding centroids of the Voronoi regions.

Table 6.2: The dataset parameters for each error intensity.

Scenario	Sensitivity ratio	Specificity ratio
1	-	0.2
2	0.2	-
3	0.2	0.2
4	-	0.4
5	0.4	-
6	0.4	0.4
7	-	0.6
8	0.6	-
9	0.6	0.6
10	-	0.8
11	0.8	-
12	0.8	0.8
13	-	0.9
14	0.9	-
15	0.9	0.9

tures [6, 15, 44], the reconstructed images (Fig.6.3g-Fig.6.3j) have interesting structural properties in the sense that they preserve many of the local ridge frequencies conveyed by the fingerprint patterns. In order to verify the accuracy of this result, we compare the phase images obtained from the features in the ground-truth (Section 6.1) with the corresponding phase estimated from the original gray-scale values (Section 5). To determine the similarity between these two iconic sets, we compute, as before, the Pearson's correlation coefficient for each image block of size 40×40. Fig. 6.4 shows the histogram of the correlation coefficients computed for all images in the ground-truth (about $21,001,800$ valid image blocks). This result shows that the reconstructed phase images are high correlated with the phase estimated from the input images. Indeed, as we can see in the histogram depicted in Fig. 6.4, about 90% of the image blocks have correlation values greater than 0.74.

6.3 Local Robustness Analysis

In this second experiment, we quantify the robustness of the reconstruction as well as the local properties of the structural quality method proposed in this work for varying values of specificity, sensitivity, and error intensity.

The dependence of the structural algorithm under random degradations concerned with dataset DB1 is depicted in Fig. 6.5, where the solid and dashed lines indicate, respectively, the average structural quality in image blocks affected and non-affected by error

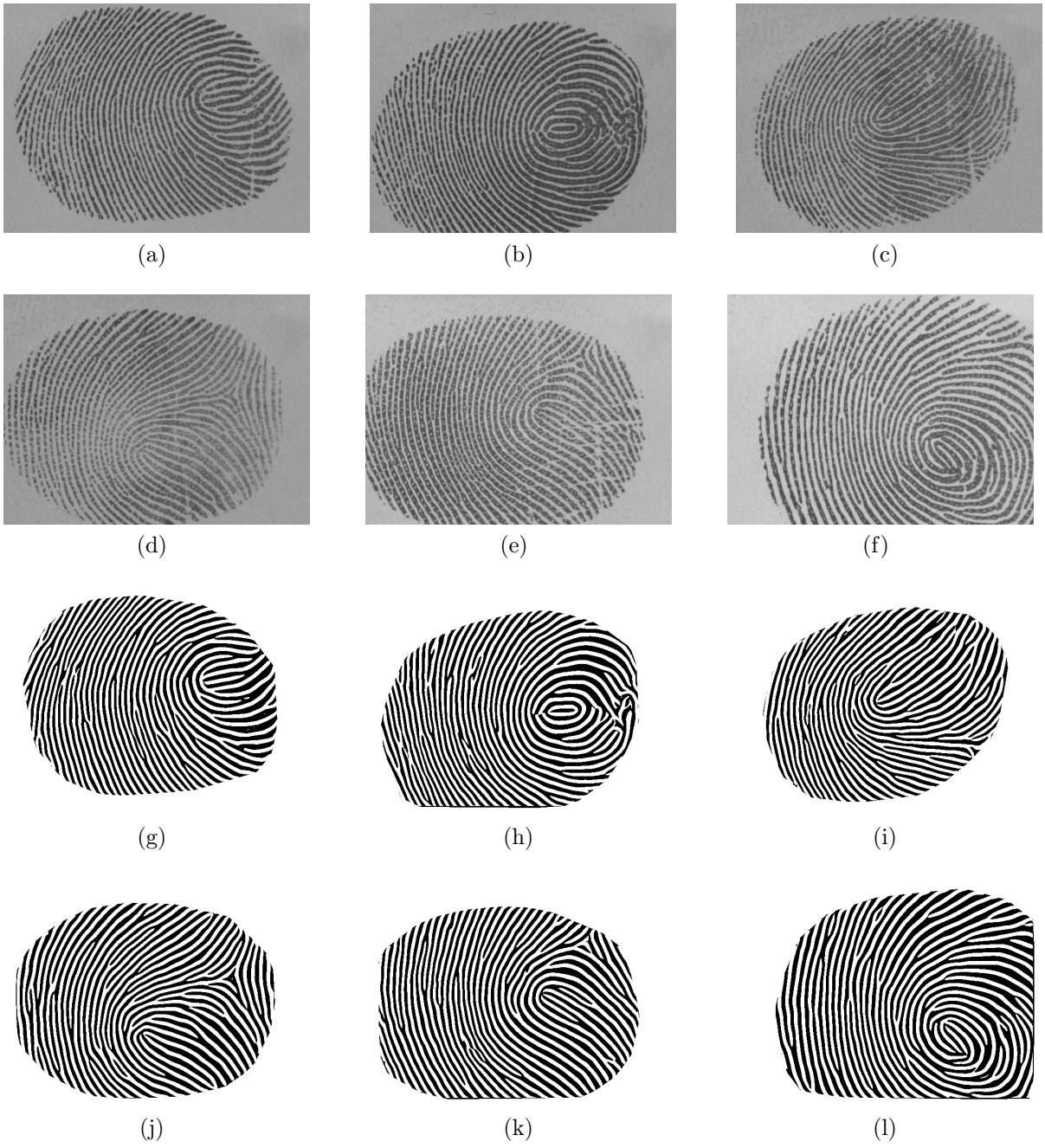

Figure 6.3: Some reconstruction examples: (a-f) Original images, and (g-l) the corresponding reconstructed phases.

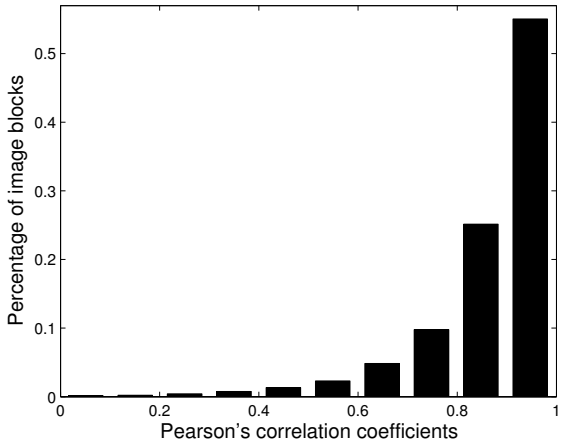

Figure 6.4: Histogram of the Pearson's correlation coefficients between the reconstructed image blocks and the corresponding original phase images for the ground-truth samples.

transformations. The black, red and blue lines indicate error scenarios with controlled specificity, sensitivity and combination of specificity and sensitivity. We recall that, as discussed in Sections 4.2 and 6.1, these types of scenarios were obtained by considering the operations of superposition and thinning. Fig. 6.5a shows the result for the fifteen first scenarios (see Table 6.2) with error intensity equal to 0.4. As we can see, there is an evident distinctness between the average structural quality of the image blocks affected and non-affected by the error transformations. Fig. 6.5b and 6.5c show the same result for scenarios relying on error intensity of 0.6 and 0.8, respectively. These results illustrate the potential of our structural quality index to properly discriminate between image blocks affected and non-affected by random noise.

The above conclusion is illustrated also in Fig. 6.6 for configurations of features with different levels of quality (Fig. 6.6a and 6.6d). Fig. 6.6a shows a feature configuration with error intensity equal to 0.4. The marked blocks used to define the regions generating this configuration is depicted in Fig. 6.6b. The structural quality map $\mathcal{Q}_2$ computed by considering the configuration in Fig. 6.6a is illustrated in Fig. 6.6c. As before, the values in Fig. 6.6c vary from black to white and correspond to the lowest and highest quality, respectively. As we can observe in this example, only the affected blocks in Fig. 6.6b have a distinguishable lower value in Fig. 6.6c. Fig. 6.6d, 6.6e and 6.6f show the same result for a configuration with error intensity equal to 0.8.

Fig. 6.7 depicts the dependence of the structural quality index, $\mathcal{Q}_2$, under intra-ridge degradations related to the dataset DB2. The black, red, and blue lines in Fig. 6.7 indicate error scenarios with controlled specificity, sensitivity and combination of both. Once again, the solid and dashed lines indicate, respectively, the average structural quality of blocks affected and non-affected by the error transformations. The behavior of the index for scenarios (see Table 6.2) with error intensities equal to 0.4, 0.6, and 0.8 is illustrated in Fig. 6.7a, 6.7b, and 6.7c, respectively. In such a case, we observe that, except for configurations with some level of sensitivity, indicated by the red lines, there is no difference between the average response of the index for regions affected and non-affected by the corresponding error transformations. This result shows that the index $\mathcal{Q}_2$ can not be used to identify such type of errors. Nevertheless, since the larger the

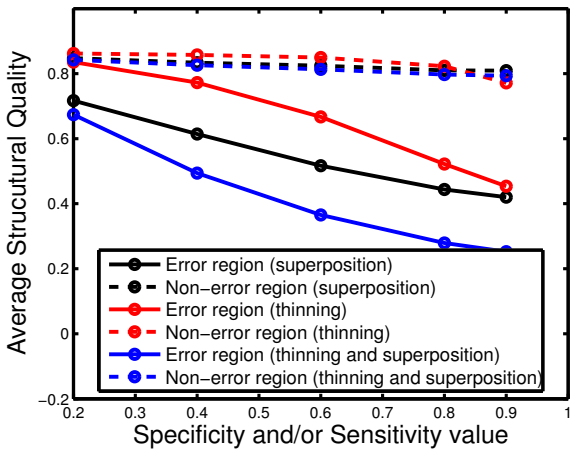

(a) Error intensity equal to 0.4

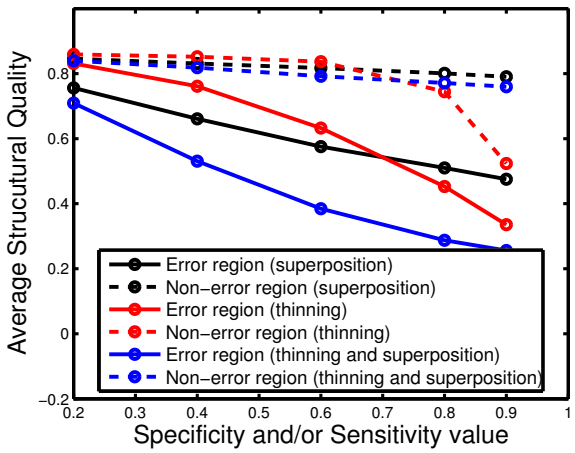

(b) Error intensity equal to 0.6

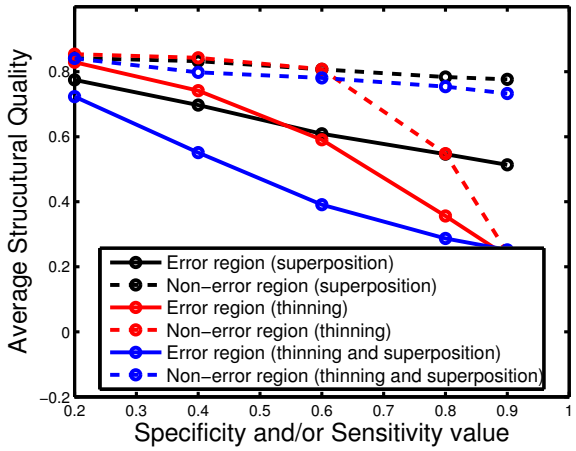

(c) Error intensity equal to 0.8

Figure 6.5: Dependence of the structural algorithm under random degradations and different error intensities.

correlation value, the more similar are the original and reconstructed phase images, we can observe that the high average values of $\mathcal{Q}_2$ reflect the effectiveness of the reconstruction approach with varying levels of intra-ridge noise.

This conclusion is illustrated again in Fig. 6.8 for a high-resolution fingerprint image (Fig. 6.8a). Fig. 6.8b, 6.8c and 6.8d show, respectively, configurations with controlled specificity, sensitivity and combination of specificity and sensitivity, where the black circles indicate the features location. Fig. 6.8e shows the phase image estimated from the gray-scale image (Fig. 6.8a). Fig. 6.8f, 6.8g and 6.8h show some reconstruction examples for error scenarios with controlled specificity (Fig. 6.8b), sensitivity (Fig. 6.8c) and combination of both (Fig. 6.8d). As we can see from Fig. 6.8, except for the configuration with a high level of sensitivity noise (Fig. 6.8g), the reconstructed phase images (Fig. 6.8f and 6.8h) are fairly consistent with the original ridges in the input image (Fig. 6.8e).

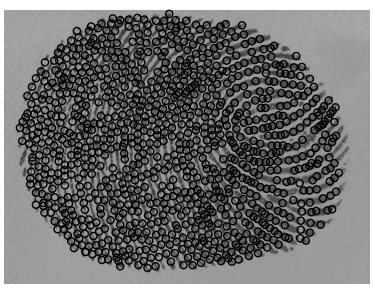

(a) Configuration with error intensity equal to 0.4.

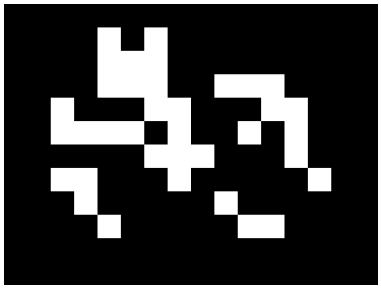

(b) Image mask representing the affected blocks by error transformations with error intensity equal to 0.4.

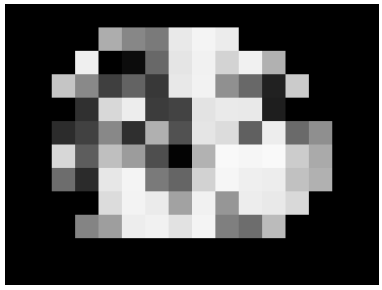

(c) Structural quality map $\mathcal{Q}_2$ obtained from configuration with error intensity equal to 0.4 (Fig. 6.6a).

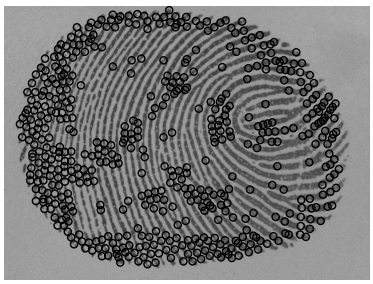

(d) Configuration with error intensity equal to 0.8

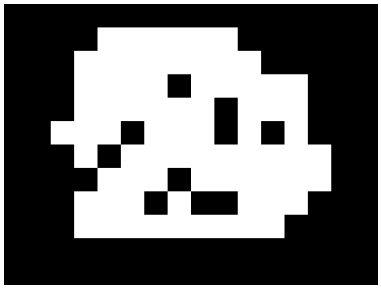

(e) Image mask representing the affected blocks by error transformations with error intensity equal to 0.8.

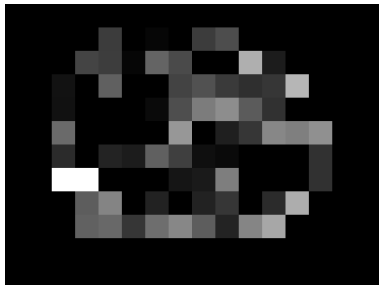

(f) Structural quality map $\mathcal{Q}_2$ obtained from configuration with error intensity equal to 0.8 (Fig. 6.6d).

Figure 6.6: Local properties of the structural quality index $\mathcal{Q}_2$ under random degradations.

6.4 Identification Performance

The aim of this third experiment is to assess the quality indexes in a fingerprint identification problem. In this case, we consider the PolyU HRF images from the second session which are matched against the $9,100$ configurations of the images from the first session, grouped in the extended datasets DB1 and DB2. Two distinct tests are considered here. First, we explore the fact that the fingerprints reconstructed by the structural algorithm are highly correlated with the corresponding phase of the input images. In this case, we compare the performance of the quality indexes when associated with a well-known fingerprint matcher [51] taking into account the minutia of the reconstructed phase images. For the second test, we consider the pore-based matcher in [61] and analyze the effectiveness of a combination of this kind of matching with the minutiae-based one where the set of minutia are obtained from the reconstructed phase images. This approach relies on the potential of the reconstruction to infer minutia from the set of available pores and use this information in a matching process.

The so-called receiver operating characteristic (ROC) curve is commonly used to analyze graphically the the effectiveness of a biometric identification system. The ROC curve plots the effectiveness of a system with reference to correct identification and misidentification. In particular, we also consider the area under this curve (AUC) which summarizes the ROC's result in a scalar amount varying from 0.5 to 1.0 and associated, respectively,

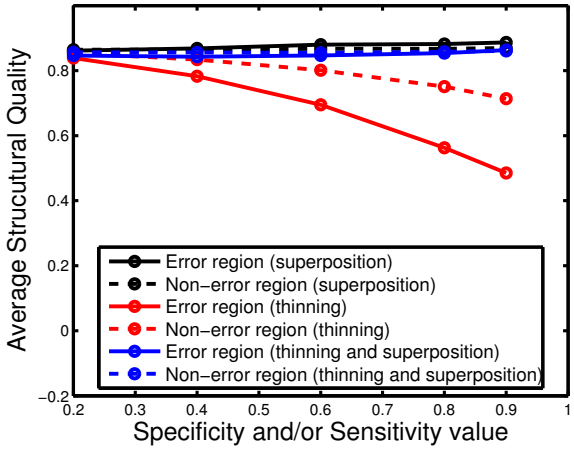

(a) Error intensity equal to 0.4

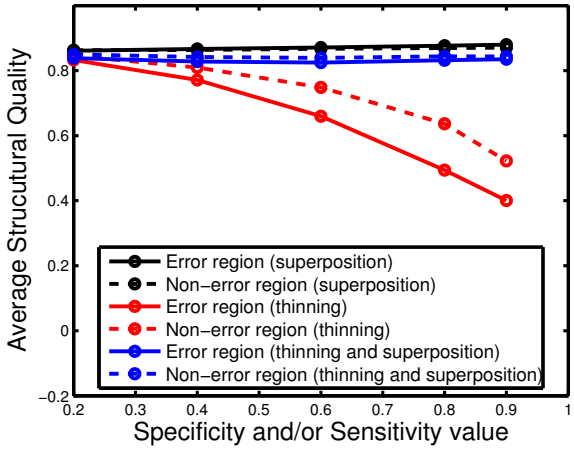

(b) Error intensity equal to 0.6

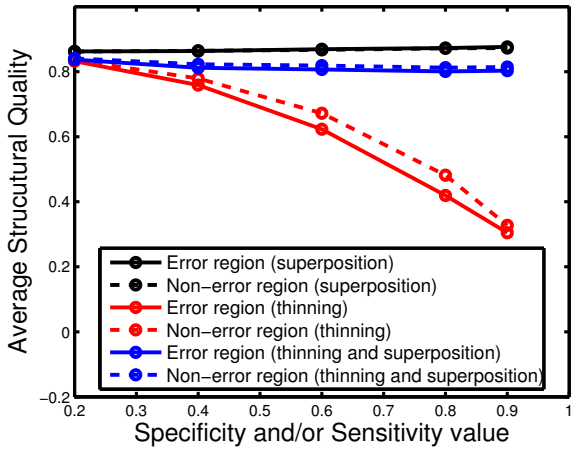

(c) Error intensity equal to 0.8

Figure 6.7: Dependence of the structural algorithm under intra-ridge degradations and different error intensities.

with worthless and perfect identification.

Fig. 6.9 shows the results of the matching with the reconstructed minutia obtained according to Section 5.2. Fig. 6.9a and 6.9b depict, respectively, the ROC curves obtained using the spatial and structural indexes. In this case, the solid and dashed lines indicate the response of the matching for high and low-quality samples, respectively. The AUC values for the spatial quality index $\mathcal{Q}_1$ (Fig. 6.9a) and associated with high and low-quality samples are, respectively, 0.77 and 0.53. For the structural index $\mathcal{Q}_2$ (Fig. 6.9a), these values are, respectively, 0.76 and 0.51. In these tests, while high-quality samples are selected by considering the values $\mathcal{Q}_1 \leq 10$ and $\mathcal{Q}_2 \geq 0.7$, low-quality ones are chosen by setting $\mathcal{Q}_1 \geq 100$ and $\mathcal{Q}_2 \leq 0.3$.

Fig. 6.10 shows the correlation among the proposed spatial (Fig. 6.10a-6.10c) and structural (Fig. 6.10d-6.10f) quality indexes, and the area under the curve obtained in the matching of the reconstructed minutia for the extended datasets. To obtain a global quality value to our local structural index, we compute the average value of all block-wise quality indexes $\mathcal{Q}_2$. The red central line in Fig. 6.10 indicates the linear surface obtained

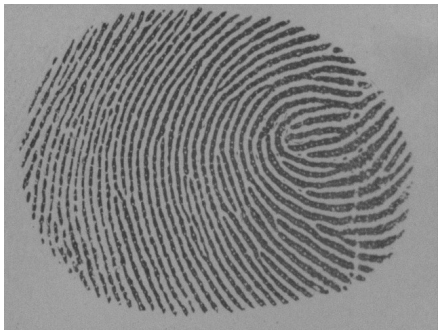

(a) Original input image.

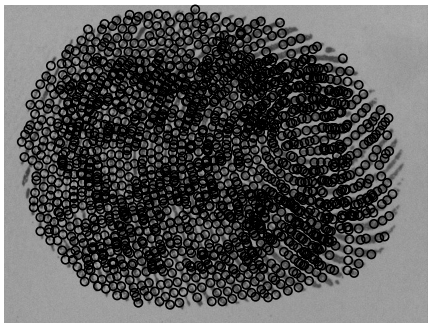

(b) Configuration with error intensity and specificity equal to 0.9 superimposed on a fingeprint image.

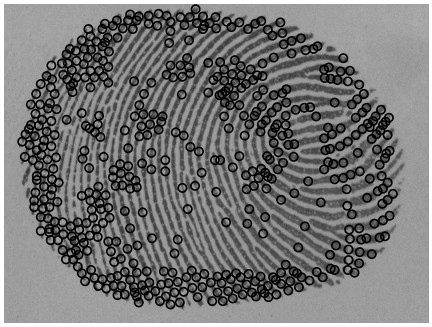

(c) Configuration with error intensity and sensitivity equal to 0.9 superimposed on a fingeprint image.

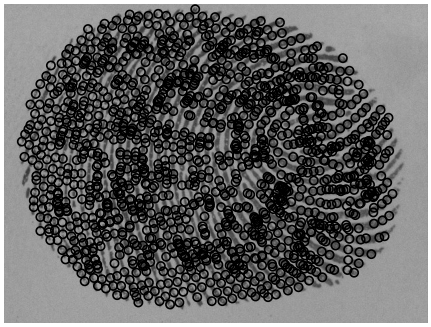

(d) Configuration with error intensity, sensitivity and specificity equal to 0.9 superimposed on a fingeprint image.

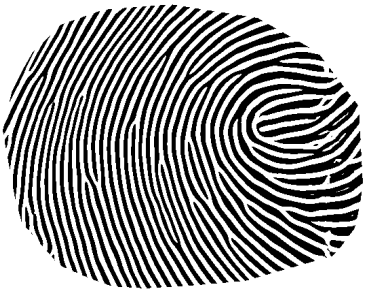

(e) Phase image estimated from input image (Fig. 6.8a).

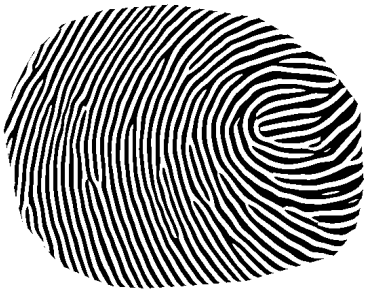

(f) Reconstructed phase image from configuration with error intensity and specificity equal to 0.9 (Fig. 6.8b)

(g) Reconstructed phase image from configuration with error intensity and sensitivity equal to 0.9 (Fig. 6.8c).

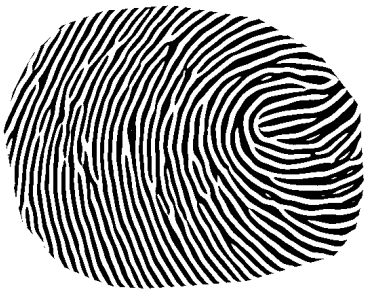

(h) Reconstructed phase image from configuration with error intensity, specificity and sensitivity equal to 0.9 (Fig. 6.8d).

Figure 6.8: Reconstruction examples for intra-ridge degradations.

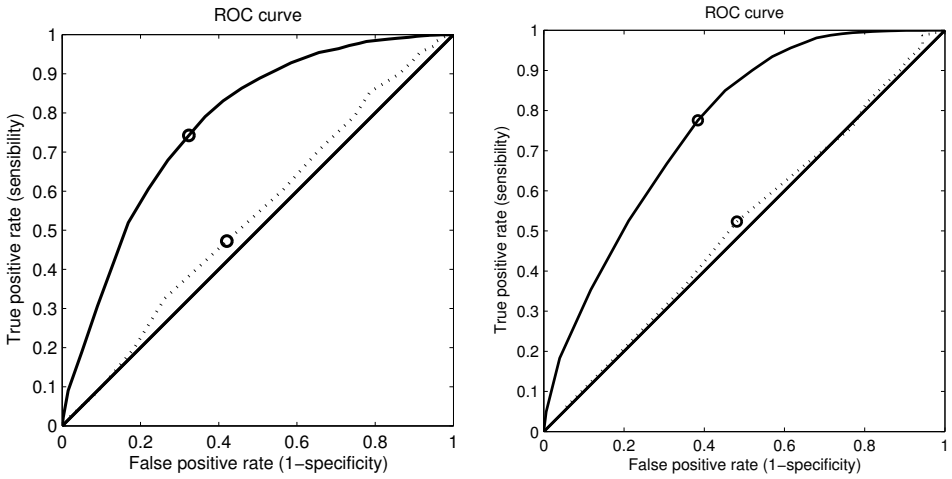

(a) Spatial quality index $\mathcal{Q}_1$ (b) Strucutural quality index $\mathcal{Q}_2$

Figure 6.9: ROC curve for spatial and structural quality indexes and two levels of quality.

by applying a robust regression [48] to the data. As we can see, there is an evident correlation among the both proposed quality indexes and the corresponding AUC obtained by matching the reconstructed minutia (correlation values corresponding to -0.89, -0.93, -0.88, 0.73, 0.94 and 0.81).

The above result confirms the potential of the proposed algorithms to predict the identification performance. To reinforce this statement, we consider now an adaptive strategy which combines the matching scores based on two different features, namely minutia and pores. This combination yields a new value $S_{\mathcal{Q}}$ related to the similarity between two images (input and template data) and depending on the quality of a given input configuration $\mathcal{S}$, as follows:

$$S_{\mathcal{Q}} = w_{\mathcal{Q}} * S_M + (1 - w_{\mathcal{Q}}) * S_P, \tag{6.1}$$

where S_M and S_P indicate the matching scores between two images and obtained, respectively, with the minutiae-based algorithm in [51] and the pore-based AFIS in [61]. In order to remap the score S_M to the same range of S_P, S_M was normalized into the interval $[0, 1]$ through the *min-max rule* [33, Chapter 7], where $min = 0$ and $max = 57$ were defined experimentally. Thus, as the quality of $\mathcal{S}$ improves, more importance is attributed to the matching score of the reconstructed minutia (S_M).

In Eq. 6.1, the importance of S_M is controlled by the quality adaptive weight $w_{\mathcal{Q}}$ which, in the test, was defined by a simple linear transformation taking into account the decision surfaces (red central lines) in Fig. 6.10 and related to the quality indexes and the identification performance:

$$w_{\mathcal{Q}} = \mathbf{m}(1, 1) * \mathcal{Q} + \mathbf{m}(2, 1), \tag{6.2}$$

where $\mathcal{Q}$ can be either the spatial quality index, $\mathcal{Q}_1$, or the structural index, $\mathcal{Q}_2$. Depending on the chosen quality index, we can have distinct values for the vector of weights $\mathbf{m}$ of dimension (2×1). Here, we set $\mathbf{m} = \left(\begin{smallmatrix} -0.0008 \\ 0.6694 \end{smallmatrix}\right)$ or $\mathbf{m} = \left(\begin{smallmatrix} 0.2130 \\ 0.4803 \end{smallmatrix}\right)$, respectively, for the

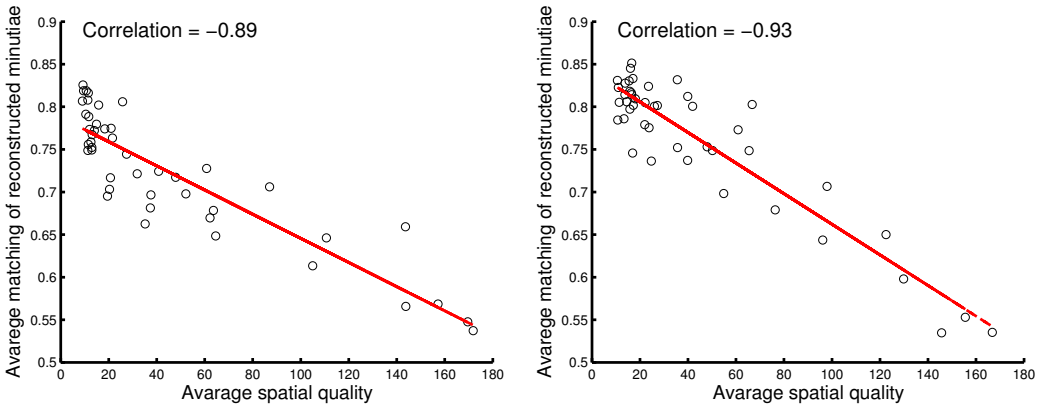

(a) Extended dataset DB1

(b) Extended dataset DB2

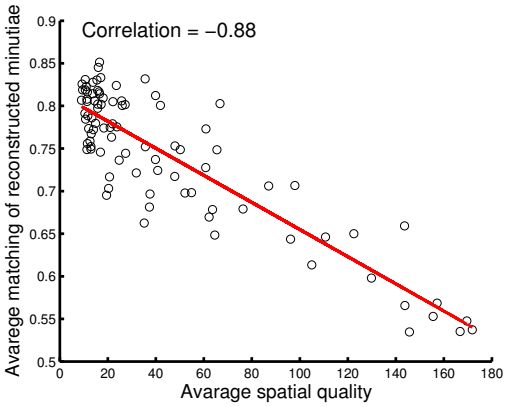

(c) Extended dataset DB1 and DB2

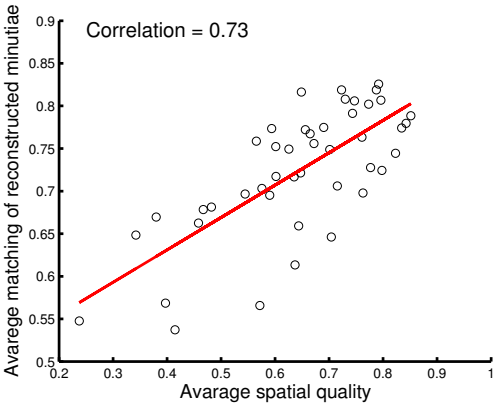

(d) Extended dataset DB1

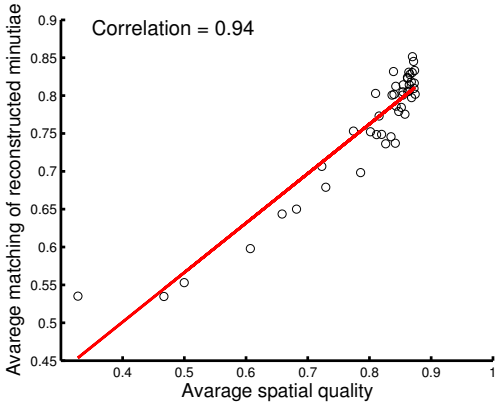

(e) Extended dataset DB2

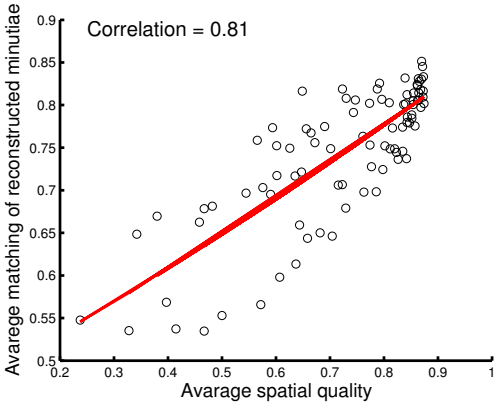

(f) Extended dataset DB1 and DB2

Figure 6.10: Correlation between the average quality indexes and the AUC obtained in all degradation scenarios of the extended datasets: (a, b, c) Spatial, and (d, e, f) Structural indexes.

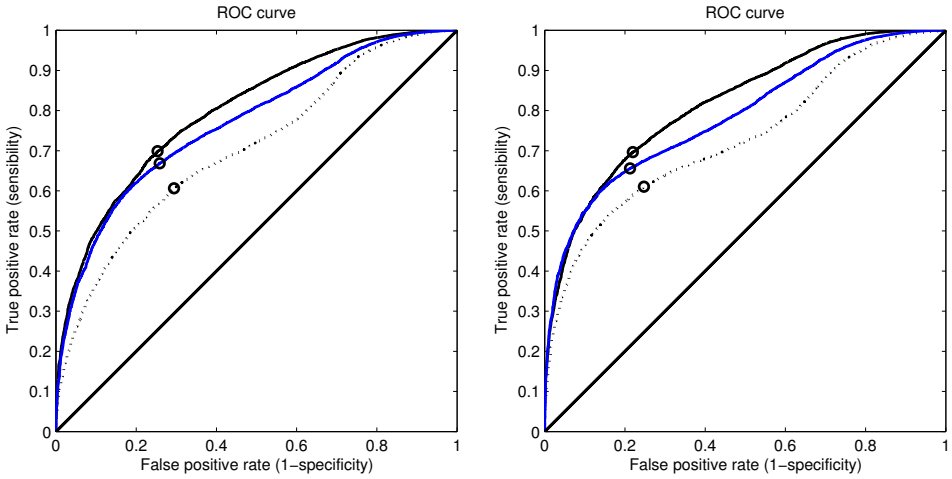

(a) Extended dataset DB1 (b) Extended dataset DB2

Figure 6.11: ROC curve for the spatial quality index.

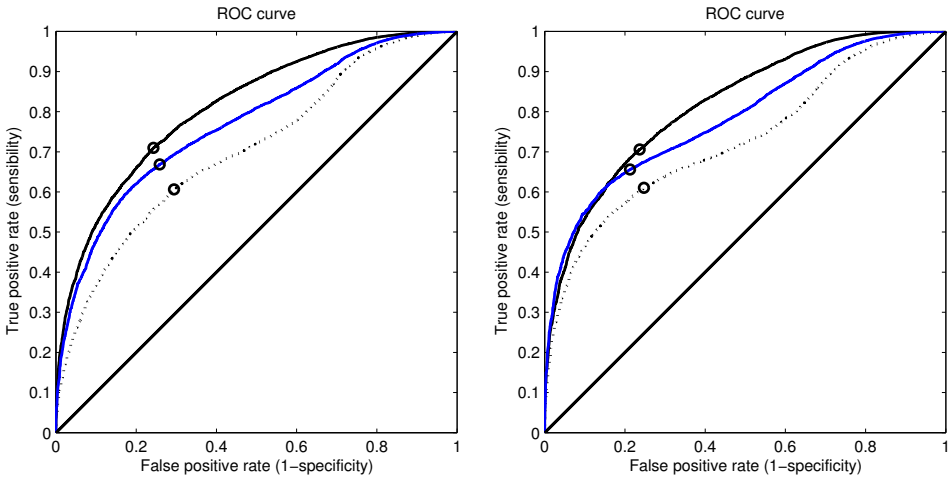

(a) Extended dataset DB1 (b) Extended dataset DB2

Figure 6.12: ROC curve for the structural quality index.

spatial and structural case.

Figure 6.11 and 6.12 show the results of the adaptive quality approach in a one-to-many fingerprint matching using, respectively, the spatial and structural quality indexes. In these cases, while the black dashed line indicates the response of the pore-based matcher proposed in [61], the black solid line shows the response of the propose adaptive strategy. The blue line indicates the behavior of the fixed combination strategy based on the sum of the unweighted values (sum rule) in Eq. 6.1. Fig. 6.11a and 6.11b show the ROC curves obtained by considering the spatial quality index for the datasets DB1 and DB2, respectively. The AUC values for the dataset DB1 (Fig. 6.11a) and associated with S_Q, sum rule and pore-based matcher are, respectively, 0.79, 0.77 and 0.70. For the dataset DB2 (Fig. 6.11b), these values are 0.81, 0.78 and 0.72. The curves concerning the structural index for the datasets DB1 and DB2 are depicted, respectively, in Fig. 6.12a and 6.12b. The values obtained for the dataset DB1 (Fig. 6.12a) and associated with the

curves concerning $S_{\mathcal{Q}}$, sum rule and pore-based matcher are, respectively, 0.81, 0.77 and 0.70. For the dataset DB2 (Fig. 6.12b), these values correspond to 0.82, 0.78 and 0.72. As wee can see from all the test cases (about $243,000$ matching instances for each quality index), the proposed adaptive combination strategy resulted in improved performance of all image quality levels, outperforming even the standard sum rule approach, especially in low image quality conditions where the performance of individual matchers may be very different. These last results illustrated also that the proposed algorithms represent indeed effective quality indexes in the sense that they can be easily used as a predictor of the performance of commonly used matching algorithms.

6.5 Discussions and Conclusions

This chapter presented contributions comprising a methodological way to assess feature-based quality indexes and improvements on the performance of pore-based matchings. To do so, we first created a new feature-based quality dataset with features configuration containing different levels of quality. We carried out experiments with this dataset to validate the proposed algorithms. The both structural and spatial algorithms have proved to be effective as a matcher predictor. From an identification point of view, we also proposed in this chapter two new approaches relying on the idea of features carrying complementary information (e.g., minutia) to the one supplied by pores, and use such a combination in well-known matching algorithms. More specifically, we showed in this part of the experiments that minutia can be inferred from the reconstructed phase images encompassed by our proposed structural algorithm and used to improve pore-based identification. We also defined an adaptive strategy to combine matching scores obtained from sets of pores and corresponding inferred minutia, based on the quality of a given features configuration. The next chapter draws some conclusions and gives a perspective of future works.

Chapter 7

Conclusions and Future Work

This work introduced a new methodology to analyze the quality of sets of level-3 fingerprint features, represented by sweat pores, and presented some experiments showing that this information may be used to improve the identification process. Our approach takes into account the spatial interrelationship between the considered features and some basic transformations involving point process and anisotropic analysis.

The increasing concern about security, privacy, and identity fraud has revived the interest in automatic human identification techniques specially in fingerprints which today have become the most popular biometric trait. As a consequence, the lack of robustness against the quality degradation affecting fingerprints is one important open issue with social and economic implications.

In this thesis, we addressed a new notion of quality assessment which considers not only the captured gray-scale image, but also the set of extracted features. Two main questions guided this study: (i) are the locations of the extracted features plausible? and (ii) is the set of extracted features coherent with other available information drawn from the captured image? To answer these questions, we proposed two new quality index algorithms with the focus on fingerprint pores and taking into account an energy-optimization standpoint. The first algorithm explored the fact that, as we shown in Section 5.1, the pores location lies at areas surrounding the centroids of Voronoi regions defined w.r.t. the original pores position. The second algorithm (Section 5.2) considered that fingerprint ridges do arise along a minimum energy path linking distinct pores.

To objectively assess the performance of these algorithms and supply the absence of a feature-based controlled quality database in biometric community, we created a dataset with features configurations containing different levels of quality. In the experiments carried out with this dataset, as we presented in Section 6.4, the two above algorithms have proved to be effective as a matcher predictor and in the definition of weights filtering out low-quality features from an identification process.

The proposed quality algorithms took into account two observations about the way fingerprints arise, namely, competitive interactions and minimum energy path linking distinct pores. From this point of view, we validated the spatial interaction of the fingerprint sweat pores and the proposed method for reconstructing the phase images from a given set of pores coordinates. In these experiments, the two contributions were tested for a consistent set of real fingerprint images and the results obtained in Section 6.2 corrobo-

rates the ideas behind the defined models. Furthermore, we also assessed the accuracy of the reconstructed phase images from an identification perspective. In such a case, we considered the set of minutia found in these images and inferred from the pores configurations and used this result in fingerprint matchings. The results reported in Section 6.4 show that this information may be used to improve the identification provided by classical pore-based matching algorithm. Since we dealt with the concept of different features (e.g., minutia and pores) carrying complementary characteristics which can be used to improve the overall matching process, we strongly believe that such a contribution offers an interesting perspective for future works.

In this sense, we are currently investigating solutions for three main shortcomings of this reconstruction process: (i) the reconstructed frequency and orientation fields are not explicitly considered, (ii) although the reconstructed images are very close to the original fingerprints, the obtained phase can be improved around the corresponding minutia, and (iii) the reconstruction step is computationally intensive.

Another promising research topic is to explore the data provided by the reconstruction step encompassed by the algorithm in Section 5.2 aiming at matching fingerprints by considering, for instance, the correspondence among ridges. In such a case, we can take advantage of the significant structural information available from the fingerprint ridges.

It is important to point out that the strategy combining the matching scores of minutia and pores features presented in Eq. 6.1 relies on a linear dependence assumption between the proposed quality indexes ($\mathcal{Q}_1$ and $\mathcal{Q}_2$) and adaptive weight $w_{\mathcal{Q}}$. So, in the future, we will evaluate other combination strategies by exploring distinct forms of dependence.

We will also investigate the use of energy-optimization observations (i.e. competitive interactions and minimum energy path linking distinct pores) for fingerprint image synthesis. Note that the synthesis of high-resolution fingerprints (i.e. fingerprint images containing level-3 features such as pores) is a very important open problem in literature. Finally, we will intend to investigate an extension of the proposed framework to other types of features, such as minutia and singular points. Since most existing AFIS are currently based on minutia, we believe that a minutiae-based version of our framework will be very useful to the biometric community.

Bibliography

[1] F. Alonso-Fernandez, J. Fierrez, J. Ortega-Garcia, J. Gonzalez-Rodriguez, H. Fronthaler, K. Kollreider, and J. Bigun. A comparative study of fingerprint image-quality estimation methods. *IEEE Transactions on Information Forensics and Security*, 2(4):734–743, Dec. 2007.

[2] L. B. Andersen and K. Thestrup-Pedersen. Sweat pore density on the fingertips of atopic patients. *British Journal of Dermatology*, 117(2):225–230, 1987.

[3] Asker M. Bazen, Gerben T. B. Verwaaijen, Sabih H. Gerez, Leo P. J. Veelenturf, and Berend Jan van der Zwaag. A correlation-based fingerprint verification system. In *ProRISC 2000, 11th Annual Workshop on Circuits, Systems and Signal Processing*, pages 205–213, 2000.

[4] Guillermo D. Canas and Steven J. Gortler. Duals of orphan-free anisotropic voronoi diagrams are embedded meshes. In *Proceedings of the Twenty-eighth Annual Symposium on Computational Geometry*, SoCG '12, pages 219–228, New York, NY, USA, 2012. ACM.

[5] Kai Cao, Eryun Liu, and A.K. Jain. Segmentation and enhancement of latent fingerprints: A coarse to fine ridgestructure dictionary. *IEEE Transactions on Pattern Analysis and Machine Intelligence*, 36(9):1847–1859, Sept 2014.

[6] R. Cappelli, D. Maio, A. Lumini, and D. Maltoni. Fingerprint image reconstruction from standard templates. *IEEE Transactions on Pattern Analysis and Machine Intelligence*, 29(9):1489–1503, 2007.

[7] Isaac Chavel. *Riemannian Geometry.* Cambridge University Press, second edition, 2006. Cambridge Books Online.

[8] Y. Chen and A. K. Jain. Beyond minutiae: A fingerprint individuality model with pattern, ridge and pores features. In *Proceedings of the International Conference on Biometrics*, ICB '09, pages 1630–1633, 2009.

[9] Yi Chen, SaratC. Dass, and AnilK. Jain. Fingerprint quality indices for predicting authentication performance. In Takeo Kanade, Anil Jain, and NaliniK. Ratha, editors, *Audio- and Video-Based Biometric Person Authentication*, volume 3546 of *Lecture Notes in Computer Science*, pages 160–170. Springer Berlin Heidelberg, 2005.

[10] H. Cummins and C. Midlo. *Finger Prints, Palms and Soles.* Dover Publications, 1943.

[11] D. J. Daley and D. Vere-Jones. *An introduction to the theory of point processes. Vol. I.* Probability and its Applications (New York). Springer-Verlag, New York, second edition, 2003. Elementary theory and methods.

[12] D. J. Daley and D. Vere-Jones. *An introduction to the theory of point processes. Vol. II.* Probability and its Applications (New York). Springer, New York, second edition, 2008. General theory and structure.

[13] Qiang Du, Vance Faber, and Max Gunzburger. Centroidal voronoi tessellations: Applications and algorithms. *SIAM Journal on Scientific Computing*, 41(4):637–676, December 1999.

[14] Qiang Du and Desheng Wang. Anisotropic centroidal voronoi tessellations and their applications. *SIAM Journal on Scientific Computing*, 26:737–761, 2005.

[15] Jianjiang Feng and Anil K. Jain. Fingerprint reconstruction: From minutiae to phase. *IEEE Transactions on Pattern Analysis and Machine Intelligence*, 33(2):209–223, 2011.

[16] Jianjiang Feng, Zhengyu Ouyang, and Anni Cai. Fingerprint matching using ridges. *Pattern Recognition*, 39(11):2131 – 2140, 2006.

[17] F. Galton. *Finger Prints.* MacMillan an Co., 1892.

[18] Nehemiah Grew. The description and use of the pores in the skin of the hands and feet, by the learned and ingenious nehemiah grew, md fellow of the college of physicians and of the royal society. *Philosophical Transactions*, 14(155-166):566–567, 1984.

[19] M. Hara and H. Toyama. Method and apparatus for matching streaked pattern image. Technical report, US Patent No. 7,295,688, 2007.

[20] E.R. Henry. *Classification and Uses of Fingerprints*, pages 54–58. London: Routledge, 1900.

[21] W. Hirsch and J. U. Schweichel. Morphological evidence concerning the problem of the skin ridge formation. *Journal of Mental Deficiency Research*, 17:58 –72, sep 1973.

[22] L. Hong, Yifei Wan, and A. Jain. Fingerprint image enhancement: algorithm and performance evaluation. *IEEE Transactions on Pattern Analysis and Machine Intelligence*, 20(8):777–789, Aug 1998.

[23] A. K. Jain, Y. Chen, and M. Demirkus. Pores and ridges: fingerprint matching using level 3 features. *IEEE Transactions on Pattern Analysis and Machine Intelligence*, 29:15–27, 2007.

[24] A. K. Jain, S. Prabhakar, L. Hong, and S. Pankanti. Filterbank-based fingerprint matching. *IEEE Transactions on Image Processing*, 9(5):846 – 859, 2000.

[25] A. K. Jain, S. Prabhakar, and S. Pankanti. On the similarity of identical twin fingerprints. *Pattern Recognition*, 35(11):2653–2663, November 2002.

[26] Suksan Jirachaweng, Zujun Hou, Wei-Yun Yau, and Vutipong Areekul. Residual orientation modeling for fingerprint enhancement and singular point detection. *Pattern Recognition*, 44(2):431 – 442, 2011.

[27] M. Kücken and C. Champod. Merkel cells and the individuality of friction ridge skin. *Journal of Theoretical Biology*, 317:229–237, 2013.

[28] M. Kücken and A. C. Newell. Fingerprint formation. *Journal of Theoretical Biology*, 235(1):71–83, 2005.

[29] François Labelle and Jonathan Richard Shewchuk. Anisotropic voronoi diagrams and guaranteed-quality anisotropic mesh generation. In *in SCG '03: Proceedings of the nineteenth annual symposium on Computational geometry*, pages 191–200. ACM Press, 2003.

[30] Sanghoon Lee, Heeseung Choi, Kyoungtaek Choi, and Jaihie Kim. Fingerprint-quality index using gradient components. *IEEE Transactions on Information Forensics and Security*, 3(4):792–800, 2008.

[31] Greg Leibon and David Letscher. Delaunay triangulations and voronoi diagrams for riemannian manifolds. In *Proceedings of the Sixteenth Annual Symposium on Computational Geometry*, SCG '00, pages 341–349, New York, NY, USA, 2000. ACM.

[32] E. Lim, Xudong Jiang, and WeiYun Yau. Fingerprint quality and validity analysis. In *Image Processing. 2002. Proceedings. 2002 International Conference on*, volume 1, pages I–469–I–472 vol.1, 2002.

[33] D. Maltoni, D. Maio, A. K. Jain, and S. Prabhakar. *Handbook of Fingerprint Recognition*. Springer, 2nd edition, 2009.

[34] K. R. Nagesh, S. Bathwal, and B. Ashoka. A preliminary study of pores on epidermal ridges: Are there any sex differences and age related changes? *Journal of Forensic and Legal Medicine*, 18(7):302–305, 2011.

[35] H. T. Nguyen. *An Introduction to Random Sets*. Chapman & Hall/CRC, London, UK, 2006.

[36] E. A. Ohler and H. Cummins. Sexual differences in breadths of epidermal ridges on finger tips and palms. *American Journal of Physical Anthropology*, 29(3):341–362, 1942.

[37] Michio Okajima and Laura Newell-Morris. Development of dermal ridges in the volar skin of fetal pigtailed macaques (macaca nemestrina). *American Journal of Anatomy*, 183(4):323–337, 1988.

[38] S. Pankanti, S. Prabhakar, and A. K. Jain. On the individuality of fingerprints. *IEEE Transactions on Pattern Analysis and Machine Intelligence*, 24:1010–1025, 2001.

[39] L. S. Penrose and P. T. Ohara. The development of the epidermal ridges. *Journal of Medical Genetics*, 10(3):201–208, set 1973.

[40] P. Prabhakar and T. Thomas. Finger vein identification based on minutiae feature extraction with spurious minutiae removal. In *Advances in Computing and Communications (ICACC), 2013 Third International Conference on*, pages 196–199, Aug 2013.

[41] Jin Qi and Mei Xie. Segmentation of fingerprint images using the gradient vector field. In *IEEE Conference on Cybernetics and Intelligent Systems 2008*, pages 543 –545, sept. 2008.

[42] Nalini K. Ratha, Shaoyun Chen, and Anil K. Jain. Adaptive flow orientation-based feature extraction in fingerprint images. *Pattern Recognition*, 28(11):1657 – 1672, 1995.

[43] A. R. Roddy and J. D. Stosz. Fingerprint features-statistical analysis and system performance estimates. *Proceedings of the IEEE*, 85(9):1390 –1421, sep 1997.

[44] A. Ross, J. Shah, and A.K. Jain. From template to image: Reconstructing fingerprints from minutiae points. *IEEE Transactions on Pattern Analysis and Machine Intelligence*, 29(4):544–560, April 2007.

[45] L. Shen, A. C. Kot, and W. M. Koo. Quality measures of fingerprint images. In *Proc. of the 3rd Int. Conf. on Audio- and Video-Based Biometric Person Authentication*, pages 266–271, 2001.

[46] B. G. Sherlock and D. M. Monro. A model for interpreting fingerprint topology. *Pattern Recognition*, 26(7):1047 – 1055, 1993.

[47] D. Simon-Zorita, J. Ortega-Garcia, J. Fierrez-Aguilar, and J. Gonzalez-Rodriguez. Image quality and position variability assessment in minutiae-based fingerprint verification. *IEEE Proceedings of Vision, Image and Signal Processing*, 150(6):402–408, Dec 2003.

[48] J. O. Street, R. J. Carroll, and D. Ruppert. A note on computing robust regression estimates via iteratively reweighted least squares. *The American Statistician*, 42:152 – 154, 1988.

[49] Prawit Sutthiwichaiporn and Vutipong Areekul. Adaptive boosted spectral filtering for progressive fingerprint enhancement. *Pattern Recognition*, 46(9):2465 – 2486, 2013.

[50] E. Tabassi and C.L. Wilson. A novel approach to fingerprint image quality. In *IEEE International Conference on Image Processing, 2005. ICIP 2005*, volume 2, pages II–37–40, Sept 2005.

[51] Elhan Tabassi, Charles L. Wilson, and Craig I. Watson. Fingerprint image quality. Technical report, NIST Report NISTIR 7151, 2004.

[52] Raoni F. S. Teixeira and Neucimar J. Leite. Unsupervised fingerprint segmentation based on multiscale directional information. In César San Martin and Sang-Woon Kim, editors, *Progress in Pattern Recognition, Image Analysis, Computer Vision, and Applications*, volume 7042 of *Lecture Notes in Computer Science*, pages 38–46. Springer Berlin Heidelberg, 2011.

[53] R.F.S. Teixeira and N.J. Leite. Improving pore extraction in high resolution fingerprint images using spatial analysis. In *IEEE International Conference on Image Processing (ICIP) 2014*, pages 4962–4966, Oct 2014.

[54] L.R. Thebaud. Systems and methods with identity verification by comparison and interpretation of skin patterns such as fingerprints. Technical report, US Patent No. 5,909,501, 1999.

[55] M. N. M. van Lieshout. *Markov Point Processes And Their Applications*. Imperial College Press (London), 2000. bibliographical data to be processed – ISBN: 1-86094-071-4 – Imperial College Press (London) – viii+175 pp.

[56] Zhou Wang, Alan C. Bovik, Hamid R. Sheikh, and Eero P. Simoncelli. Image quality assessment: From error visibility to structural similarity. *IEEE Transactions on Image Processing*, 13(4):600–612, 2004.

[57] Wencheng Yang, Jiankun Hu, and Song Wang. The effect of spurious and missing minutiae on delaunay triangulation based on its application to fingerprint authentication. In *11th International Conference on Fuzzy Systems and Knowledge Discovery (FSKD) 2014*, pages 995–999, Aug 2014.

[58] L. Yount. *Forensic Science: From Fibers to Fingerprints*. Milestones in discovery and invention. Facts On File, Incorporated, 2007.

[59] Eun-Kyung Yun and Sung-Bae Cho. Adaptive fingerprint enhancement with fingerprint image quality analysis. *Image and Vision Computing*, 24:101–110, 2006.

[60] Q. Zhao, D. Zhang, L. Zhang, and N. Luo. Adaptive fingerprint pore modeling and extraction. *Pattern Recognition*, 43(8):2833 – 2844, 2010.

[61] Q. Zhao, L. Zhang, D. Zhang, and N. Luo. Direct pore matching for fingerprint recognition. In *Proceedings of the Third International Conference on Advances in Biometrics*, ICB '09, pages 597–606, Berlin, Heidelberg, 2009. Springer-Verlag.

[62] Qijun Zhao, David Zhang, Lei Zhang, and Nan Luo. Polyu high-resolution fingerprint database. `http://www4.comp.polyu.edu.hk/~biometrics/HRF/HRF_oldnew.htm`. Accessed: 2015-10-17.

[63] Y. Zhu, S. C. Dass, and A. K. Jain. Statistical models for assessing the individuality. *IEEE Transactions on Information Forensics and Security*, 2(3):391–401, 2007.